Spectral methods for the equations of classical density-functional theory: Relaxation dynamics of microscopic films

Petr Yatsyshin, Nikos Savva, and Serafim Kalliadasis

Citation: The Journal of Chemical Physics **136**, 124113 (2012); doi: 10.1063/1.3697471
View online: http://dx.doi.org/10.1063/1.3697471
View Table of Contents: http://scitation.aip.org/content/aip/journal/jcp/136/12?ver=pdfcov
Published by the AIP Publishing

Spectral methods for the equations of classical density-functional theory: Relaxation dynamics of microscopic films

Petr Yatsyshin, Nikos Savva, and Serafim Kalliadasis
Department of Chemical Engineering, Imperial College London, London SW7 2AZ, United Kingdom

(Received 18 October 2011; accepted 7 March 2012; published online 29 March 2012)

We propose a numerical scheme based on the Chebyshev pseudo-spectral collocation method for solving the integral and integro-differential equations of the density-functional theory and its dynamic extension. We demonstrate the exponential convergence of our scheme, which typically requires much fewer discretization points to achieve the same accuracy compared to conventional methods. This discretization scheme can also incorporate the asymptotic behavior of the density, which can be of interest in the investigation of open systems. Our scheme is complemented with a numerical continuation algorithm and an appropriate time stepping algorithm, thus constituting a complete tool for an efficient and accurate calculation of phase diagrams and dynamic phenomena. To illustrate the numerical methodology, we consider an argon-like fluid adsorbed on a Lennard-Jones planar wall. First, we obtain a set of phase diagrams corresponding to the equilibrium adsorption and compare our results obtained from different approximations to the hard sphere part of the free energy functional. Using principles from the theory of sub-critical dynamic phase field models, we formulate the time-dependent equations which describe the evolution of the adsorbed film. Through dynamic considerations we interpret the phase diagrams in terms of their stability. Simulations of various wetting and drying scenarios allow us to rationalize the dynamic behavior of the system and its relation to the equilibrium properties of wetting and drying. © *2012 American Institute of Physics*. [http://dx.doi.org/10.1063/1.3697471]

I. INTRODUCTION

One of the most widely used methods for the study of the microscopic structure of fluids is density-functional theory (DFT). It is based on first principles and offers an increasingly popular compromise between computationally costly molecular dynamics simulations and phenomenological approaches. We consider here the wetting of a flat, attractive-repulsive substrate with a fluid as a prototype model for DFT. The bulk density of the fluid is below that of the saturated vapor at the given temperature and its intermolecular potential has an attractive part. Typically, a thin liquid-like film is adsorbed on the substrate. Depending on the temperature, T, and the pressure in the bulk of the fluid, P, the coverage of the wall with the liquid-like film can vary from a few molecular diameters up to macroscopic length-scales, as the bulk pressure approaches that of the saturated vapor. The understanding of wetting by liquid film has important implications to other more complex problems of wetting in different geometries,[1–8] as well as droplet formation.[9,10]

As was first pointed out by Cahn[11] using heuristic arguments and later calculated for the first time by Ebner and Saam,[12] there can exist several possible scenarios regarding the wetting of flat substrates by a fluid. These works stirred much discussion in the literature in the 1980s and the early 1990s and greatly stimulated the development of DFT. Since then, many theoretical and experimental works have subsequently appeared in the literature that looked at wetting through the DFT formalism (see, for example, Refs. 7 and 13–17 for comprehensive reviews of the area).

There exist extensive DFT calculations of equilibrium adsorption for Lennard-Jones (LJ) fluids on various substrates. The development of *ab initio* potentials which accurately model real substrates,[18,19] has allowed DFT simulations of wetting phenomena which compare well with experimental data.[20,21] More recently, a further improvement in the quantitative agreement of DFT calculations with molecular dynamics simulations was achieved,[22,23] by employing techniques that allow the inclusion of information about the correlation structure of the fluid into the attractive part of the free energy functional.[24–27]

In general, the governing equations of DFT are highly nonlinear and not easily amenable to analytical work, which is partly due to the presence of non-local integral terms. As a result, numerical approaches are usually more appropriate to investigate DFT problems. Typically, the non-local terms are computed using the trapezoidal rule, as, for example, in the study of Dhawan *et al.*,[28] who compared various DFT approximations in relation to the associated wetting transitions, by utilizing a uniform grid with 20 or more discretization points per molecular diameter, which naturally becomes increasingly inefficient as the film thickness grows. An alternative method has been proposed by Roth,[29] in which he exploited the convolution-like form of the integral terms and utilized the Fourier Transform to compute them. However, this scheme, like the trapezoidal rule, has an algebraic convergence and is, in principle, equivalent to a higher-order Simpson rule. Regarding the resulting discretized equations, they are typically solved using Picard's iteration (see, e.g., Refs. 8, 10, 29 and 30), but this method usually exhibits slow

convergence, requiring also special care in preparing the input for each successive iteration.[29] Regarding the computation of the wetting isotherms and phase diagrams, in general, simple parameter continuation techniques together with some specialized tricks for the initial guess were employed in early works (e.g., Ref. 28), until the pseudo-arclength continuation algorithm together with Newton's iterations was introduced in DFT calculations by Frink and Salinger in their investigation of porous media.[31]

The vast majority of the work on DFT has been devoted to equilibrium configurations. However, the study of dynamic phenomena through the dynamic extension of DFT (DDFT), apart from studying dynamic interfacial phenomena occurring at the nanoscale, can also impact the areas of front propagation (e.g., Refs. 9, 32, and 33) and the development of phase field models (e.g., Refs. 34 and 35). For phase field models in particular, the free energy functionals of DFT directly follow from the statistical mechanical considerations of molecular-level interactions, which can be viewed as a first-principles generalization of the otherwise phenomenological phase field models based on the Ginzburg-Landau functionals. The square gradient approximation, in particular, allows to retrieve the Ginzburg-Landau-type functional within DFT.[36]

While most of work on DDFT focus on colloidal systems,[37–40] the underlying assumptions of DDFT allow for a generalization to molecular fluids, as was initially suggested by Evans[14] and further developed by Chan and Finken[41] and Archer.[42] Thiele *et al.*[43] applied these DDFT concepts to open systems by investigating the de-wetting of colloidal suspensions, whereby the conservation equations of DDFT for colloid particles were coupled with the dissipative equation for the solvent.

The purpose of the current work is to propose a model-invariant numerical methodology for solving the typical equilibrium and dynamic DFT equations and for illustration purposes it is applied to the equilibrium and dynamic behavior of a molecular fluid undergoing a wetting transition. The methodology is distinctly different from the above-mentioned studies. It is based on a spectral collocation method on a generally non-uniform grid, which allows the concentration of discretization points in regions where the density exhibits rapid variations. Such regions can be approximately located for most problems *a priori*, from physical considerations. On the other hand, in regions where the density profile does not change significantly, a moderate number of discretization points would save computation time. An additional advantage of our scheme is that it allows us to obtain a global rational interpolant,[44,45] which can give the density at arbitrary locations within our computational domain.

The convolution-type integrals characteristic of DFT equations are approximated by the highly accurate Clenshaw–Curtis quadrature, which is known to exhibit an exponential convergence rate for sufficiently smooth integrands.[46,47] Our scheme is made even more efficient by reducing the convolution-type integral evaluations to matrix-vector products through appropriately forming an integration matrix for that purpose, which is constant for a given computational grid. We also directly incorporate into our numerical method the results of an asymptotic analysis of the density profiles, which further improves the accuracy of the non-local term associated with the attractive interactions.

The details of our approximation for the free energy functional are given in Sec. II. Our model system consists of a single-component LJ fluid adsorbed on a flat horizontal substrate. The value of chemical potential is below that of liquid-vapor coexistence at any given temperature. We use a perturbative approach with the purely repulsive hard sphere fluid being the reference system and the attractive LJ interactions imposed perturbatively within the mean field approximation. Our model for the substrate potential follows the original calculations of Ebner and Saam,[12] using the LJ potential integrated over the infinite volume of the substrate. Section III contains a discussion on the dynamic extension of DFT for open systems. The DDFT equation we employ for the time-dependent density contains a dissipative term to allow for an open system. A similar approach has been used by Thiele *et al.*[43] In fact, this DDFT approach follows closely the ideas originally developed for phase-field models of moving contact lines.[34]

In Sec. IV we provide the model equations for the planar, one-dimensional (1D) system to be used as means to illustrate the scheme we develop. In Sec. V we analyze the asymptotic behavior of the density for small and large distances from the wall. This allows us to approximate the infinite convolution-like integral accounting for the attractive interactions for finite-domain calculations.

The details of our numerical method to solve the equilibrium and dynamic equations are outlined in Sec. VI. The method allows for a straightforward application to different DFT formalisms, as well as to problems with different geometries and of higher dimensions. When supplemented with a numerical continuation algorithm, which we also briefly discuss, it constitutes a complete tool for systematically investigating any equilibrium configuration in DFT. To illustrate the method in Sec. VII we show how it can be applied to the calculation of equilibrium wetting isotherms and the complete pre-wetting lines, along with their spinodals, for various values of the strength parameter of the wall-fluid potential, as well as for different DFTs.

In Sec. VIII we consider the relaxation dynamics of the density profiles. We show that the wetting isotherms have an appealing interpretation in terms of stability which confirms the expectations based on the analysis of the grand canonical potential. The different types of wetting equilibria correspond to distinct scenarios of the dynamic behavior of the liquid film. As a matter of fact, the observation of this dynamic system reveals the presence of an equilibrium first-order wetting transition. We close with conclusions and perspectives in Sec. IX.

II. FREE-ENERGY FUNCTIONAL

In the grand canonical DFT treatment, the equilibrium density, $\rho(\mathbf{r})$, of a single-component fluid in an external potential, $V_{\text{ext}}(\mathbf{r})$, minimizes the grand free-energy

functional $\Omega[\rho(\mathbf{r})]$:

$$\Omega\left[\rho\left(\mathbf{r}\right)\right] = F\left[\rho(\mathbf{r})\right] - \mu \int d\mathbf{r}\rho\left(\mathbf{r}\right), \tag{1}$$

where the functional $F[\rho(\mathbf{r})]$ is the fluid free energy and μ is the chemical potential. The minimization of $\Omega[\rho(\mathbf{r})]$ is achieved by the function $\rho(\mathbf{r})$ that satisfies the Euler-Lagrange equation,

$$\frac{\delta F\left[\rho(\mathbf{r})\right]}{\delta\rho\left(\mathbf{r}\right)} - \mu = 0. \tag{2}$$

This formalism requires as input the free-energy functional of the fluid, $F[\rho(\mathbf{r})]$.[36] Here we employ an approach in which the purely repulsive, hard sphere fluid is assumed to be the reference system, with the attractive interactions imposed perturbatively, which has proven to be rather successful in the range of gas- and liquid-like bulk densities.[36] With this approach, the free energy functional commonly has four distinct parts: (a) the ideal gas part, (b) the reference hard sphere part, which accounts for the short-range repulsive effects induced by molecular packing, (c) the part due to the external potential, and (d) the perturbative part, which accounts for the attractive interactions:

$$F\left[\rho(\mathbf{r})\right] = \int d\mathbf{r}\, f_{\mathrm{id}}(\rho(\mathbf{r})) + F_{\mathrm{hs}}[\rho(\mathbf{r})] + \int d\mathbf{r}\rho(\mathbf{r})V_{\mathrm{ext}}(\mathbf{r}) + \frac{1}{2}\int d\mathbf{r}\int d\mathbf{r}'\rho(\mathbf{r})\rho(\mathbf{r}')g(\mathbf{r},\mathbf{r}')\varphi_{\mathrm{attr}}(|\mathbf{r}-\mathbf{r}'|), \tag{3}$$

where $g(\mathbf{r}, \mathbf{r}')$ is the pair correlation function of the nonuniform fluid, $\varphi_{\mathrm{attr}}(r)$ is the attractive pair potential, $f_{\mathrm{id}}(\rho) = k_{\mathrm{B}}T\rho\left(\ln\left(\lambda\rho\right) - 1\right)$ is given exactly by the local functional of the density, with k_{B} being the Boltzmann constant and λ being the thermal wavelength.

The correlation structure of the liquid-like fluid is known to be mainly determined by the short-range repulsions due to molecular packing.[48] This allows us to account for attractive interactions in a mean-field fashion, incorporating all nonlocal correlations into the repulsive part of the functional and setting

$$g(\mathbf{r}, \mathbf{r}') = \Theta(|\mathbf{r} - \mathbf{r}'| - \sigma), \tag{4}$$

where σ is the molecular diameter and $\Theta(x)$ is the Heaviside step function. Such prescription for the pair correlation function allows one naturally to use $\varphi_{\mathrm{attr}}(r)$ from the Barker and Henderson split of the 6−12 LJ pair potential, which was originally proposed for uniform systems:[49]

$$\varphi_{\mathrm{attr}}(r) = \begin{cases} 0, & r \le \sigma \\ \varphi_{\sigma}^{\mathrm{LJ}}, & r > \sigma \end{cases}, \tag{5}$$

where

$$\varphi_{\sigma}^{\mathrm{LJ}}(r) = 4\varepsilon\left[\left(\frac{\sigma}{r}\right)^{12} - \left(\frac{\sigma}{r}\right)^{6}\right], \tag{6}$$

where ε is a measure of the strength of the potential. There exist more sophisticated approximations for the attractive part of the free-energy functional which go beyond the mean-field treatment, either by the (*ad hoc*) parameter-fitting in the Weeks-Chandler-Anderson[50,51] or the Barker-Henderson[24,49] prescriptions or through a truncated functional Taylor expansion of the free energy around that of a uniform fluid.[23]

The hard sphere free-energy functional $F_{\mathrm{hs}}\left[\rho\left(\mathbf{r}\right)\right]$ is not known exactly and must be approximated. In the theories for single-component molecular fluids (e.g., Refs. 52 and 53) the starting point is to choose the configurational part of the free energy, obtained from the thermodynamic equation of state, which is defined as

$$\psi\left(\rho\right) = \frac{f_{\mathrm{hs}}\left(\rho\right) - f_{\mathrm{id}}\left(\rho\right)}{\rho}, \tag{7}$$

where f_{hs} and f_{id} are the thermodynamic free energies per particle of the hard sphere fluid and ideal gas, respectively. In this work, we use the Carnahan and Starling[54] equation of state for the hard sphere fluid, with

$$\psi\left(\rho\right) = k_{\mathrm{B}}T\frac{\eta\left(4-3\eta\right)}{\left(1-\eta\right)^{2}}, \quad \eta = \pi\sigma^{3}\rho/6, \tag{8}$$

where η is the packing fraction for the hard spheres of diameter σ. An extensive review of various equations of state along with the analysis of the corresponding phase diagrams can be found in Ref. 48.

In the simplest approximation for the free-energy functional for hard spheres, the so-called local density approximation (LDA), the functional is obtained by allowing for the $\mathbf{r}$-dependence of the number density in Eq. (8) and using the expression, $F_{\mathrm{hs}}^{\mathrm{LDA}}\left[\rho\right] = \int d\mathbf{r}\rho\left(\mathbf{r}\right)\psi\left(\rho\left(\mathbf{r}\right)\right)$. Such an approach does not account properly for the repulsive interactions, which play a defining role in forming the fluid-wall interface as well as the shape of the density profile near the wall. There exist extensive studies in the literature analyzing the limits of applicability of LDA (see, e.g., Refs. 15, 36, and 55) and it is widely accepted that LDA can adequately describe the free liquid-vapor interface under certain conditions.[56] For example, in adsorption problems, we find that, in principle, LDA can be used to describe the liquid-vapor interface if the wall effects are negligible, as is the case for systems with large values of the wall coverage, or, equivalently, when the bulk density approaches that of the coexisting gas.[55] However, since LDA cannot properly account for structuring in the fluid, it fails to describe the near-wall oscillatory behavior of the density profiles, given that it can affect appreciably the liquid-vapor interface for small values of coverage and/or temperatures.[55,57] Thus the applicability of LDA to adsorption problems is rather limited.

To account for the wall effects on the liquid-vapor interface, we use the weighted density approximation (WDA),[58] which can be viewed as a method of coarse-graining the fluid density. This is achieved by introducing an "averaged" density, $\bar{\rho}\left(\mathbf{r}\right)$, in the expression for the configurational part of the free energy, Eq. (8), which is defined as

$$\bar{\rho}(\mathbf{r}) = \int d\mathbf{r}'\rho(\mathbf{r}+\mathbf{r}')W(\mathbf{r}'), \tag{9}$$

where $W(\mathbf{r})$ is some weight function, the choice of which depends on the specific version of WDA. The hard sphere

functional, F_{hs}, in Eq. (3) is given by

$$F_{\text{hs}}[\rho] = \int d\mathbf{r}\rho(\mathbf{r})\psi(\bar{\rho}(\mathbf{r})). \tag{10}$$

Here we use the prescription for the weight function due to Tarazona and Evans:[52]

$$W(\mathbf{r}) = \frac{3}{4\pi\sigma^3}\Theta(\sigma - r). \tag{11}$$

The weight is selected so that the direct correlation function of the hard sphere fluid obtained from Eq. (10) via the functional differentiation route correctly reproduces one of the main features of its uniform counterpart, namely a step at the distance of σ.[57] The hard sphere free energy functional given by Eqs. (8)–(11) takes into account the non-local, short-ranged correlations in the fluid. The same free-energy functional has been used in some recent works of other authors, e.g., Refs. 59 and 60.

There exist, in fact, numerous prescriptions for the free-energy functional of the hard sphere fluids, but a universally applicable one is presently elusive. Different models are usually constructed by requiring the functional to reproduce well-known results in some established limiting cases.[28,29] Hence, the choice of the equation of state and the appropriate coarse-graining procedure is dictated by the problem under consideration (see, e.g., Refs. 29 and 48 for comprehensive reviews).

Rather sophisticated prescriptions for the free-energy functional of hard spheres are known under the general name of the Fundamental Measure Theory (FMT) class.[29,48] The FMT prescriptions for $F_{\text{hs}}[\rho(\mathbf{r})]$ can be constructed by requiring that the hard sphere functional satisfies simultaneously a low density, or a low dimensional, limit together with an appropriate bulk thermodynamic condition, which can be given in the form of an equation of state.[29,61,62] The original FMT was constructed by Rosenfeld in Ref. 61 using the exact zero density limit of the hard sphere free energy functional and the scaled particle theory equation in the bulk, which is equivalent to the Percus-Yevick equation of state. A more accurate equation of state, namely that of Carnahan and Starling[54] has been incorporated into the FMT family of approximations for $F_{\text{hs}}[\rho(\mathbf{r})]$ by Tarazona in Ref. 63 for a single-component hard sphere fluid, and by Roth *et al.* in Ref. 62 for both a single-component fluid and an additive mixture of hard sphere fluids. The latter FMT approximation is referred to as the White Bear FMT. As it follows the same equation of state in the bulk limit as the version of WDA which we employ in the present work, it is possible to compare the results predicted by both directly and gain an estimate as to which extent the excluded volume correlations incorporated into WDA can represent the near-wall behavior of the fluid as obtained from a more sophisticated approximation known to provide simulation quality results for a purely repulsive hard sphere fluid.[29]

With the White Bear FMT (Ref. 62) the expression for the hard sphere free energy functional is given in the form

$$F_{\text{hs}} = k_{\text{B}}T\int d\mathbf{r}\Phi(\{n_\alpha(\mathbf{r})\}), \tag{12}$$

where $\Phi(\{n_\alpha(\mathbf{r})\})$ is a function of the variables $n_\alpha(\mathbf{r})$:

$$\Phi(\{n_\alpha(\mathbf{r})\}) = -n_0\ln(1-n_3) + \frac{n_1n_2 - \mathbf{n}_1\mathbf{n}_2}{1-n_3} + \left(n_2^3 - 3n_2\mathbf{n}_2\mathbf{n}_2\right)\frac{n_3 + (1-n_3)^2\ln(1-n_3)}{36\pi n_3^2(1-n_3)^2}. \tag{13}$$

The so-called fundamental measures, $n_\alpha(\mathbf{r})$, are obtained from the density, $\rho(\mathbf{r})$, by integrating with a corresponding weight:

$$n_\alpha = \int d\mathbf{r}\rho(\mathbf{r}-\mathbf{r}')\omega_\alpha(\mathbf{r}'). \tag{14}$$

The weight functions are given by

$$\omega_3(\mathbf{r}) = \Theta(\sigma/2 - r), \tag{15a}$$

$$\omega_2(\mathbf{r}) = \delta(\sigma/2 - r), \tag{15b}$$

$$\omega_1(\mathbf{r}) = \omega_2(\mathbf{r})/2\pi\sigma, \tag{15c}$$

$$\omega_0(\mathbf{r}) = \omega_2(\mathbf{r})/\pi\sigma^2, \tag{15d}$$

$$\boldsymbol{\omega}_2(\mathbf{r}) = \delta(\sigma/2 - r)\mathbf{r}/r, \tag{15e}$$

$$\boldsymbol{\omega}_1(\mathbf{r}) = \omega_2(\mathbf{r})/2\pi\sigma, \tag{15f}$$

where $\delta(\mathbf{r})$ is the Dirac's delta-function. The details on how an FMT functional can be implemented in various geometries can be found in the review paper by Roth.[29] We shall provide an FMT-based calculation of the equilibrium density profiles for illustration purposes and to demonstrate that the WDA prescription for F_{hs}, which we will use for our dynamic calculations, is capable of capturing the physics of the investigated phenomena. The comparison between the results obtained using the WDA prescription for $F_{\text{hs}}[\rho(\mathbf{r})]$ given by Eqs. (8)–(11) and the results obtained using the White Bear FMT prescription given by Eqs. (12)–(15) is done in Sec. VII. It is shown that in the problems of liquid adsorption, the WDA-based hard sphere functional $F_{\text{hs}}[\rho(\mathbf{r})]$ provides a good prototypical model and leads to density profiles with a similar near-wall behavior as those predicted by a more sophisticated approximation for $F_{\text{hs}}[\rho(\mathbf{r})]$, such as the one given by the White Bear version of FMT.

Finally, to account for planar wall effects, we introduce an external potential in the form[64]

$$V_{\text{ext}}(z) = E_{\text{w}}\int_{-\infty}^{\infty}dx'\int_{-\infty}^{\infty}dy'\int_{-\infty}^{0}dz' \times\varphi_{\sigma_{\text{w}}}^{LJ}\left(\sqrt{x'^2 + y'^2 + (z-z')^2}\right), \tag{16}$$

where z is the distance in the lateral direction. The energy parameter of the wall is given by $E_{\text{w}} = 4\pi\varepsilon_{\text{w}}\rho_{\text{w}}\sigma_{\text{w}}^3$ with ρ_{w} being the uniform solid density and ε_{w} and σ_{w} being the parameters of the LJ wall potential. Throughout this study we

fixed $\sigma_w = 1.25\sigma$. By integrating Eq. (16), we finally obtain a 3−9 LJ potential:

$$V_{ext}(z) = E_w\left(-\frac{1}{6}\left(\frac{\sigma_w}{z}\right)^3 + \frac{1}{45}\left(\frac{\sigma_w}{z}\right)^9\right). \quad (17)$$

It important to emphasize that there exist highly accurate models for the substrate potentials of some alkaline metals,[18,19] but the potential given by Eq. (17) suffices for the purpose of illustrating our method.

III. DYNAMICS OF ADSORBED FILM

Non-equilibrium systems, i.e., systems whose density does not satisfy Eq. (2), are much less understood compared to equilibrium ones, since a rigorous statistical theory for non-equilibrium processes, which is able to account for dynamic molecular-level interactions, has not been developed yet. This modeling difficulty is typically remedied in large-scale systems by employing semi-phenomenological phase field models.[34,35] Nevertheless, it is generally agreed that if the dynamical system is not far from equilibrium, the expressions for the grand free-energy functional, Eq. (1), and the corresponding Helmholtz free energy functional, Eq. (3), are expected to hold with reasonable accuracy, if the time-dependent $\rho(\mathbf{r}, t)$ is substituted in place of the equilibrium $\rho(\mathbf{r})$. A detailed account of the DDFT formalism based on this assumption of proximity to equilibrium can be found in Refs. 14, 41, 42, 65, and 66.

In this study we investigate a liquid film adsorbed on a wall, which forms an open dynamical system in contact with an infinite thermostat. The first process assumed to contribute to the evolution of such a system is a dissipative one, which can be described by the equation:[34,35]

$$\frac{\partial \rho(\mathbf{r}, t)}{\partial t} = -\zeta \frac{\delta \Omega[\rho(\mathbf{r})]}{\delta \rho(\mathbf{r}, t)}, \quad (18)$$

where ζ determines the rate of relaxation to equilibrium.

Alternatively, one can consider a second mechanism contributing to the dynamics, namely the conservation of mass and an associated diffusive flow. For a system at equilibrium, $\delta F/\delta\rho(\mathbf{r})$ is equal to a constant, the chemical potential, μ. Out of equilibrium μ is both spatially and time dependent and its gradient can be viewed as a force acting on the fluid particles, which drives the system to equilibrium. The flux due to this force is then given by $\mathbf{j}(\mathbf{r}, t) = -\gamma\rho(\mathbf{r}, t)\nabla\mu(\mathbf{r}, t)$, where we have introduced the positive mobility constant γ,[14,67] which is related to the diffusion coefficient, D, through $\gamma = k_B T D$. The evolution of the fluid density is described by the continuity equation, namely $\partial\rho(\mathbf{r}, t)/\partial t = -\nabla\mathbf{j}(\mathbf{r}, t)$, which becomes

$$\frac{\partial \rho(\mathbf{r}, t)}{\partial t} = \gamma\nabla\left(\rho(\mathbf{r}, t)\nabla\frac{\delta F[\rho(\mathbf{r}', t)]}{\delta\rho(\mathbf{r}, t)}\right), \quad (19)$$

upon substitution of $\mu(\mathbf{r}, t)$ by the expression in Eq. (2). Equation (19) was first introduced by Evans[14] and later justified by more rigorous arguments by Dietrich *et al.*,[67] Marconi and Tarazona[68] and Chan and Frinken.[41]

In the present study we assume that both the dissipative and conservative mechanisms contribute to the evolution of the fluid density, so that the dynamic equation takes the from

$$\frac{\partial \rho(\mathbf{r}, t)}{\partial t} = \gamma\nabla\left(\rho(\mathbf{r}, t)\nabla\frac{\delta F[\rho(\mathbf{r}', t)]}{\delta\rho(\mathbf{r}, t)}\right) - \zeta\left(\frac{\delta F[\rho(\mathbf{r}', t)]}{\delta\rho(\mathbf{r}, t)} - \mu\right), \quad (20)$$

where, again, F is given by Eq. (3) and μ is the chemical potential attained by the system in the long time limit. A similar dynamic equation has been employed in the study of colloidal dewetting by Thiele *et al.*[43] Naturally, the stationary solutions of Eq. (20) correspond to the solutions predicted by the equilibrium DFT, Eq. (2). As we shall see later, even though the final equilibrium is set by Eq. (2), the way this state is attained depends on the relative importance of dissipation to diffusion, measured by the ratio γ/ζ. Noteworthy is also that the two distinct processes discussed above are otherwise referred to as model A, for the dissipative, and model B, for the conservative equation, in the general dynamic universality class.[34,35]

IV. GOVERNING EQUATIONS

In what follows we consider the non-dimensional form of the governing equations, by scaling the quantities of interest as shown in Table I. It is evident from Eq. (17) that the density of the fluid adsorbed on the planar wall varies only in the lateral direction. Hence, the equilibrium and dynamic equations can be reduced to their 1D form by integrating over the transverse coordinates.

The attractive potential is obtained by integrating Eq. (5), $\varphi(z) = \int_0^\infty\int_0^\infty \varphi_{attr}\left(\sqrt{x^2+y^2+z^2}\right)dxdy$:

$$\varphi(z) = \begin{cases} -\frac{6\pi}{5}, & \text{if } |z| \le 1 \\ 4\pi\left(\frac{1}{5z^{10}} - \frac{1}{2z^4}\right), & \text{if } |z| > 1 \end{cases}. \quad (21)$$

The variation of the hard sphere free energy, Eq. (10), with respect to $\rho(z)$ is

$$\mu_{hs}[\rho(z)] = \psi(\bar{\rho}(z)) + \int_0^\infty W(z')\rho(z')\psi'_\rho(\bar{\rho}(z))dz', \quad (22)$$

where ψ'_ρ is the derivative of the right-hand side of Eq. (8) with respect to ρ, and the 1D coarse-grained density $\bar{\rho}$

TABLE I. Units for equations in dimensionless form.

Unit	Measure
Length	σ
Energy	ε
Temperature	ε/k_B
Time	$\gamma^{-1}\sigma^2/\varepsilon$

is given by

$$\bar{\rho}(z) = \int_0^\infty W(z')\rho(z+z')dz' \tag{23}$$

with

$$W(z) = \frac{3}{4}(1-z^2)\Theta(1-|z|). \tag{24}$$

By combining Eqs. (21)–(24), we express the intrinsic chemical potential $\delta F/\delta\rho$ as

$$\frac{\delta F}{\delta \rho} = T\ln\rho(z) + \mu_{\text{hs}}[\rho(z)] + \mathcal{E}[\rho;z] + V_{\text{ext}}(z), \tag{25}$$

where $\mathcal{E}[\rho;z]$ is the interaction energy,

$$\mathcal{E}[\rho;z] = \int_0^\infty \varphi(z-z')\rho(z')dz'. \tag{26}$$

The equilibrium states of the system are given by Eq. (2). With respect to Eq. (25) it takes the form

$$T\ln\rho(z) + \mu_{\text{hs}}[\rho(z)] + \mathcal{E}[\rho;z] + V_{\text{ext}}(z) - \mu = 0, \tag{27}$$

whereas the equation for the evolution of the 1D density profile, Eq. (20), takes the form

$$\frac{\partial\rho}{\partial t} = \frac{\partial}{\partial z}\left(\rho\frac{\partial}{\partial z}\frac{\delta F}{\delta\rho}\right) - \kappa\left(\frac{\delta F}{\delta\rho} - \mu\right), \tag{28}$$

where $\kappa = \sigma^5\zeta/\gamma$ measures the relative importance of the dissipative and conservative terms.

V. ASYMPTOTIC ANALYSIS

We will first analyze the asymptotic behavior of the fluid density for small and large distances from the wall, as this information will be incorporated in the numerics, and, more specifically, in the non-local term, in order to produce more accurate results. As previously noted, throughout this paper the bulk fluid density is assumed to be below that of the coexisting gas for the temperatures we consider. Near the wall, the fluid density must vanish, unless one considers wall potentials with a cutoff (e.g., Ref. 28). Far from the wall, the fluid no longer "feels" its effects and approaches a uniform value, ρ_{B}; the rate of decay towards ρ_{B}, however, is dependent on the interplay between the wall potential and the attractive fluid pair-potential. The analysis that follows is expected to be valid both for equilibrium and dynamics, due to our assumption of relatively small deviations from equilibrium. As we shall later see, the bulk properties of the fluid determine the properties of equilibrium adsorption, as well as the dynamic behavior of the adsorbed film.

Consider Eq. (27) as $z \to 0$. Since we require $\rho(z) \to 0$ as $z \to 0$, we must balance two competing singular terms, namely $\ln\rho(z)$ and an $O(-1/z^9)$ term due to $V_{\text{ext}}(z)$, Eq. (17), which results to a super-exponential decay of the density, i.e., $\rho \propto \exp(-1/z^9)$ as $z \to 0$. The difficulties in the discretization of a density with such behavior are remedied by regularizing the near-wall behavior with the change of variable, $\rho(z) = f(z)\exp(-V_{\text{ext}}(z)/T)$. This can be viewed as an explicit separation of the ideal and the excess-over-ideal contributions to the fluid density.

Consider now Eq. (27) as $z \to \infty$. For the equilibrium problem, the density $\rho(z)$ should asymptotically approach the constant value ρ_{B} in the bulk of the fluid, due to the decaying wall effects with z. In order to determine the asymptotic behavior of $\rho(z)$ in the bulk of the fluid, first consider the non-local attractive term in Eq. (27), whose asymptotic behavior is

$$\int_0^\infty \varphi(z-z')\rho(z')dz' \sim c + O\left(\frac{1}{z^3}\right), \tag{29}$$

where c is some constant. Since for large z the leading term of the wall potential, Eq. (17), is also $O(1/z^3)$, it follows from Eq. (27) that the density must behave like

$$\rho(z) \sim \rho_{\text{B}} + \frac{\alpha}{z^3} + O\left(\frac{1}{z^4}\right), \tag{30}$$

as $z \to \infty$, where α is a constant to be determined. Further details on the asymptotic behavior of density profiles with liquid-vapor interfaces and the associated phenomena may be found in Ref. 69. By substituting Eq. (30) into Eq. (27), expanding asymptotically and matching orders of z, we obtain algebraic equations for the parameters in Eq. (30). More specifically, from the $O(z^0)$ terms we obtain a nonlinear equation for the density in the bulk, ρ_{B}:

$$\mu = T\ln\rho_{\text{B}} + \psi(\rho_{\text{B}}) + \rho_{\text{B}}\psi'_\rho(\rho_{\text{B}}) - \frac{32\pi}{9}\rho_{\text{B}}. \tag{31}$$

Note, that at coexistence Eq. (31) for ρ_{B} corresponds to the thermodynamic condition of chemical equilibrium satisfied by the liquid and gas densities. For the present study of wetting by gas, for given T and μ we select ρ_{B} to be the solution to Eq. (31), which is below the coexistence value for the density, determined from the conditions of mechanical and chemical equilibrium (e.g., Ref. 28).

By matching the $O(z^{-3})$ terms of Eq. (27), we obtain an expression for the constant α, namely

$$\alpha = \left(\frac{2\pi}{3}\rho_{\text{B}} - \frac{E_{\text{w}}\sigma_w^3}{6}\right)\Big/\frac{d\mu}{d\rho_{\text{B}}}, \tag{32}$$

where $d\mu/d\rho_{\text{B}}$ corresponds to the derivative of the right-hand side of of Eq. (31) with respect to ρ_{B}.

The asymptotics of $\rho(z)$, Eq. (30), may be utilized when formulating the problem numerically on a finite but sufficiently large domain, $[0, L]$ with $L \gg 1$, whereby the non-local term, Eq. (26), is split into two integrals, from 0 to L and from L to infinity, estimating the second using Eq. (30),

$$\mathcal{E}[\rho;z] \approx \int_0^L \varphi(z-z')\rho(z')dz' + \int_L^\infty \varphi(z-z')\left(\rho_{\text{B}} + \frac{\alpha}{z'^3}\right)dz' + O\left(\frac{1}{L^4}\right). \tag{33}$$

In the end, both integrals are to be evaluated numerically, but through this splitting we avoid the unnecessary discretization of the density for very large distances from the wall, since $\rho(z)$ rapidly decays to ρ_{B}. At the same time, we also obtain highly accurate results since we also incorporate into this evaluation the second-order term of the asymptotics of $\rho(z)$.

VI. NUMERICAL SCHEME

We solve Eqs. (27) and (28) with $\delta F/\delta\rho$ given by Eqs. (25) and (26) numerically on $[0, L]$ using the rational pseudo spectral collocation method for the spatial discretization. While its implementation, especially for the non-local terms, is not as straightforward as, say, implementing Simpson's rule, the typically exponential convergence of the scheme as the number of discretization points increases allows for a highly accurate calculation, while maintaining a low computational cost, when compared to conventional methods. The methodology which underlies our scheme has originally been developed mostly for partial differential equations, but its main ideas allow for an application to a class of integral and integro-differential equations typical of DFT and DDFT problems.

In this section, we outline the scheme we developed, explaining how such methods can be applied in the spatial discretization of Eqs. (27) and (28). Our scheme is general in the sense that it can be configured to any type of DFT approximation, both on bounded or unbounded domains. To illustrate the main concepts, we only consider one-dimensional problems, but our scheme can be extended to higher-dimensional problems through a careful generalization of the ideas we present, with the intention to tackle rather efficiently some of the computationally stringent problems of DFT. Leaving aside all the theoretical details of spectral methods (for a more detailed account see, e.g., Refs. 44, 70, and 71), we focus on providing an overview of the key ingredients needed to practically implement our scheme.

For an N-point discretization scheme, the density is to be determined at a prescribed set of collocation points, z_k, with $k = 1, \ldots, N$, so that $\hat{\rho}_k = \rho(z_k)$ satisfy the governing equations. An important aspect of our method is that by choosing appropriately the $\{z_k\}$, one can prescribe a ratio of polynomials, $R_N(z)$, to represent the density over the whole computational domain, which also satisfies $\hat{\rho}_k = R_N(z_k)$. Thus, all mathematical operations like differentiation and integration are performed on $R_N(z)$ via matrix-vector products with the discrete data, $\hat{\rho}_k$. The foundations of this method, which is known to exhibit exponential convergence, were laid by Baltensperger *et al.*[70] and further expanded by Berrut and Trefethen.[71] The global interpolating function is conveniently expressed in the so-called barycentric form,[70]

$$R_N(z) = \frac{\sum_{k=1}^{N}{}' \frac{(-1)^k}{z - z_k}\hat{\rho}_k}{\sum_{k=1}^{N}{}' \frac{(-1)^k}{z - z_k}}, \tag{34}$$

where the primes indicate that the first and last terms in the sums are to be multiplied by 1/2. The global interpolant, $R_N(z)$ is typically reduced to a ratio of polynomials, unless the $\{z_k\}$ correspond to the Chebyshev collocation points, $\{x_k\}$, defined as

$$x_k = \cos\frac{(k-1)\pi}{N-1}, \quad k = 1, \ldots, N, \tag{35}$$

in which case Eq. (34) becomes an $(N-1)$-degree polynomial. However, if the $\{z_k\}$ result from a transformation of the corresponding set of $\{x_k\}$ it has been shown[70,71] that provided that the map from $\{x_k\}$ to $\{z_k\}$ is conformal and that the approximated function is sufficiently smooth, $R_N(z)$ exponentially converges to $\rho(z)$ as N increases, i.e., $\|\rho(z) - R_N(z)\| = O(A^{-N})$, for some $A > 1$.

While there is some freedom to choose the map from the $\{x_k\}$ to the $\{z_k\}$, it is typically chosen such that more collocation points are clustered in the vicinity of steep gradients in $\rho(z)$, so that these are well resolved. For the configurations studied in this work with Eqs. (27) and (28), we anticipate sharp variations near the wall due to the competition between the repulsive and the attractive fluid-substrate interactions. Thus, the steepest gradient is expected in the vicinity of the minimum of $V_{\text{ext}}(z)$, at $z_0 = (2/5)^{1/6}\sigma_w \approx 0.94\sigma_w$, where the density profile attains its global maximum. The density maximum is accompanied by a sequence of oscillations which capture the fine structure of the fluid near the wall and decay exponentially towards the bulk. The oscillations become more pronounced for strongly attractive substrates and/or lower temperatures, inducing eventually a layering or a freezing transition, in which the fluid exhibits a solid-like, long-ranged ordering. This effect is manifested in the density profile as a sequence of isolated peaks separated by distances of approximately one molecular diameter.[72]

Therefore, in order to adequately capture the oscillations of the profile, the mesh should be dense in the near-wall region of the physical domain. We obtain the collocation points on the physical domain, $z \in [0, L]$ by mapping N Chebyshev points, $x \in [-1, 1]$, using the map

$$z = g(x) = \frac{p(1+x)}{1 - x + 2p/L}, \tag{36}$$

where p is an empirically chosen parameter, so that $1 < p \ll L$. With this transformation, about half of the Chebyshev points are mapped to the interval $[0, p]$; the other half are mapped to $[p, L]$. This allows us to avoid the wasteful concentration of the collocation points in the bulk of the fluid, where the density varies slowly. The parameter p is typically calibrated by a few trial calculations so that the near-wall oscillations of the density profile fall within $[0, p]$. However, the results of our calculations are not sensitive to p, which only affects slightly the convergence rate. It is important to emphasize that at the liquid-vapor interface $\rho(z)$ does not vary as steeply as near the wall and the way the collocation points are distributed is sufficient to resolve its transition to the bulk gas value of the density. Noteworthy is also that other types of maps could have been employed (e.g., Ref. 73), but the one given by Eq. (36) is sufficient for our purposes.

One can also take the limit $L \to \infty$, essentially considering the whole physical domain $[0, \infty)$, as done, for example, in other problems where spectral methods are employed.[44] In that case, the asymptotic behavior of $\rho(z)$ is no longer required, but one has to modify the discretized equations accordingly, by discarding the respective zero contributions at infinity, which would be now treated as a true boundary condition. However, it may be desirable (e.g., for the study of layering transitions[74]) to perform the computations on a finite domain, in order to resolve accurately the oscillatory behavior of the density profile near the wall, avoiding the unnecessary

placement of collocation points in a region where the fluid density is nearly constant.

In the methodology developed here, the mth derivative of $\rho(z)$ is approximated by that of the global interpolant $R_N(z)$, which can be computed by multiplying the discretized data, $\hat{\rho}_k$ with the differentiation matrix $D^{(m)}$,

$$\left.\frac{d^m \rho(z)}{dz^m}\right|_{z=z_k} \approx R_N^{(m)}(z_k) = \sum_{j=1}^{N} D_{kj}^{(m)} \hat{\rho}_j. \tag{37}$$

Given the set of collocation points $\{z_k\}$, the entries $D_{ij}^{(m)}$ can be obtained by differentiating Eq. (34) directly, but these can be done more efficiently and accurately by recursive formulas for $D_{ij}^{(m)}$. These expressions for the entries of $D_{ij}^{(m)}$, as well as the computer code for their calculation may be found in Refs. 45 and 73.

The integrals associated with DFT calculations may be computed efficiently with the Clenshaw–Curtis quadrature, which is also related to pseudospectral methods and exhibits exponential convergence.[46] This method for evaluating integrals has been originally developed for computing integrals of functions discretized on the Chebyshev grid. For example, for a function $f(x)$ defined on $[-1, 1]$, this integral can be computed on the N-point Chebyshev grid, Eq. (35), as

$$\int_{-1}^{+1} f(x)\,dx \approx \sum_{k=1}^{N} \hat{f}_k w_k, \tag{38}$$

where $\hat{f}_k$ is the discrete data of $f(x)$ at $x = x_k$ and w_k are the constant Clenshaw–Curtis weights, chosen so that the integral of the interpolating polynomial associated with the $\{x_k\}$ is evaluated exactly. The computation of the $\{w_k\}$ is done efficiently via the fast Fourier Transform, as pointed out in Ref. 46, whereby the necessary MATLAB code is also given. In our computations, the integrals we consider are to be evaluated on domains that are different from $[-1, 1]$, but this can be easily remedied by appropriate changes in the integration variable.

Just like differentiation operations are carried out by matrix-vector products with the discrete data, $\hat{\rho}_k$, it is desirable to form matrix operators for the convolution-like integrals of DFT. Naturally, these matrices are dependent on the grid employed, but need to be determined only once for the entire calculation. As we shall demonstrate, these considerations are model-invariant and are applicable to other types of DFT approximations, be it LDA, WDA, or the more modern alternative based on FMT (e.g., Ref. 29).

Generally, in DFT computations one is interested in evaluating convolution-like integrals, on a subinterval of the physical domain, $[a(z), b(z)] \subset [0, L]$,

$$I(z) = \int_{a(z)}^{b(z)} Q(z - z')\rho(z')dz', \tag{39}$$

where the integral kernel, $Q(z)$, is a known function. Given the global approximant to $\rho(z)$ represented explicitly by the data $\hat{\rho}_k$ at the collocation points z_k, we are interested in finding the discrete approximation to $I(z)$ at the same set of points, $\hat{I}_k = I(z_k)$, with $k = 1, \ldots, N$.

Computing the discrete $\{\hat{I}_k\}$ is equivalent to performing N integrations, one for each of the discretization points, and it is possible to compute these components via a linear operator, $\hat{I}_k = \sum_{j=1}^{N} J_{kj}\hat{\rho}_j$, where J is an $N \times N$ matrix. For every integral we make a change of variable by conformally mapping $[-1, 1]$ onto the domain of integration $[a(z_k), b(z_k)]$, so that we may apply the Clenshaw–Curtis quadrature to evaluate the integral. While there can exist many suitable candidates for performing this change of variable, e.g., maps that concentrate more points in the vicinity of sharp gradients, in our case we have linearly mapped an M Chebyshev points, $\tilde{x} \in [-1, 1]$ onto each domain $[a(z_k), b(z_k)]$:

$$z = d_k(\tilde{x}) = \frac{b_k - a_k}{2}\tilde{x} + \frac{a_k + b_k}{2}, \tag{40}$$

where $a_k = a(z_k)$ and $b_k = b(z_k)$. Obviously, the number of points used to compute these integrals, M, does not affect the final size of the matrix operator, J. However, we have found that the convergence of the scheme improves for any $M > N$. Given also that the computation of $\hat{I}_k$ is done once, we generally used a large number of points, typically $M = 2N$.

To compute the integral at each interval $[a_k, b_k]$, we defined the intermediate collocation points $y_{kq} = d_k(\tilde{x}_q)$, with $q = 1, \ldots, M$. A crucial step in our scheme is the evaluation of the density appearing in the integrand at the y_{kq}, which is done by utilizing the rational interpolant of $\rho(z)$, Eq. (34). Then, by rearranging the indices we eventually obtain an expression for the entries of the integrating operator, which depends only on the collocation grid, $\{z_k\}$. The entries of the integrating operator, J_{ij}, are given by

$$J_{ij} = \begin{cases} J'_{ij}/2, & \text{for } j = 1 \text{ and } j = N \\ J'_{ij}, & \text{otherwise} \end{cases}, \tag{41}$$

with

$$J'_{ij} = \frac{(b_i - a_i)(-1)^j}{2} \sum_{q=1}^{M} \frac{\tilde{w}_q Q(z_i - y_{iq})}{y_{iq} - z_j} \times \left(\sum_{m=1}^{N}{}' \frac{(-1)^m}{y_{iq} - z_m} \right)^{-1}, \tag{42}$$

where $\{\tilde{w}_q\}$ are the Clenshaw–Curtis weights corresponding to $\{\tilde{x}_q\}$.

As an example, we show how the integrating operator given in Eq. (41) may be used to calculate the non-local term $\mathcal{E}[\rho; z]$ due to attractive interactions, Eq. (26). From the asymptotic analysis, it follows that we need to compute the first term of Eq. (33) via suitable matrix-vector products. More specifically, by accounting for the three branches of $\varphi(z)$, Eq. (21), the first term of Eq. (33) may be

written as

$$\int_0^L \varphi(z-z')\rho(z')dz' = \int_{\max(0,z-1)}^{z-1} \phi_{\text{out}}(z-z')\rho(z')dz' + \phi_{\text{in}} \int_{\max(0,z-1)}^{\min(z+1,L)} \rho(z')dz' + \int_{\min(z+1,L)}^{L} \phi_{\text{out}}(z-z')\rho(z')dz', \tag{43}$$

where ϕ_{in} and $\phi_{\text{out}}(z)$ denote the constant "inner" ($|z| \leq 1$) and the smoothly decaying "outer" ($|z| \geq 1$) branches of $\varphi(z)$ in Eq. (21), respectively. Thus, the integrating operator for the discrete version of Eq. (43) is essentially the sum of the three integration matrices constructed for each of its three constitutive terms, by using Eq. (41). With these considerations, we complete the presentation of our discretization scheme, since in a similar manner, any 1D convolution-type integral may be conveniently cast as a matrix operating on the discrete values of $\rho(z)$.

VII. WETTING AT EQUILIBRIUM

After discretizing the equilibrium equation, Eq. (27), we obtain a set of N nonlinear equations, which are solved by the standard Newton's iteration algorithm. The implementation of non-local terms by matrix operators facilitates the calculation of the Jacobian whose entries are evaluated analytically, which is known to accelerate the convergence of the Newton's algorithm compared to a Jacobian obtained by finite differences.[75] In our computations, we typically use $N = 300$ grid points for both equilibrium and dynamic configurations. For a domain of length $L = 80$, this corresponds to an average of less than 4 collocation points per molecular diameter, which is to be contrasted with 20 mesh points per molecular diameter for conventional methods.[28] The Newton's scheme usually converges in less than 4 iterations for the chosen tolerance of 10^{-10} for the target function.

Before embarking on a detailed discussion of the equilibrium configurations, we present a few representative density profiles demonstrating the exponential convergence of our scheme. Figure 1(a) shows the two coexisting density profiles, which correspond to a prewetting transition, as well as a density profile of a thicker film, whose bulk density is close to that of the coexisting gas. The latter was added for illustration purposes. The near-wall oscillations are captured due to the non-local repulsive part of the WDA free-energy functional. The inset in Fig. 1(a) demonstrates the exponential rate of convergence with the number N of discretization points. Considering the profile calculated using $N = 1000$ collocation points as a reference one, we define the error, $E(N)$, for the profile calculation with $N < 1000$ as

$$E(N) = \sqrt{\sum_{k=1}^{1000} [R_N(\chi_k) - R_{1000}(\chi_k)]^2}, \tag{44}$$

where $R_N(x)$ is defined by Eq. (34) and is evaluated at $\chi_k = L(k-1)/999$.

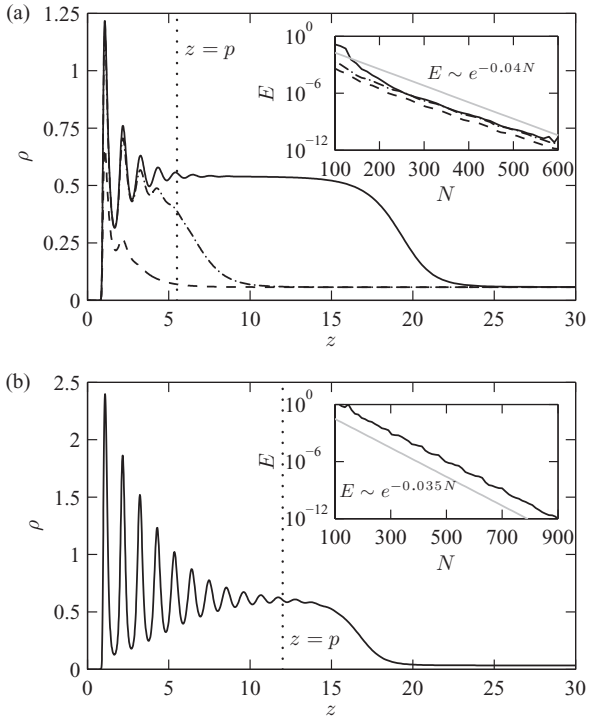

FIG. 1. Demonstration of the exponential convergence for the numerical scheme. The profiles are calculated using WDA. (a) Dashed and dashed-dotted curves denote coexisting density profiles corresponding to a prewetting transition ($\Delta\mu_0 = -0.008$), whereas the profile plotted by the solid line corresponds to a thick film ($\Delta\mu \approx -10^{-4}$) at the same temperature. $T = 0.85T_{\text{crit}}$, $E_{\text{w}} = 9.82$, with $L = 80$ and $p = 5.5$. (b) Highly structured profile of a fluid adsorbed on a strongly attractive substrate at $T = 0.85T_{\text{crit}}$, $\Delta\mu \approx -10^{-3}$, $E_{\text{w}} = 12.2$ with $L = 80$ and $p = 12$. The vertical dotted lines in (a) and (b) demarcate the $z = p$ line, dividing the computational domain so that half of the collocation points lie in $[0, p]$. The insets show the corresponding decay of the error, $E(N)$, together with the corresponding decay rates obtained by least-squares fitting (gray lines).

Figure 1(b) shows a profile for an extreme case of a fluid at low temperature whose chemical potential is close to coexistence, together with the error, $E(N)$, plotted in the inset. The density profile is highly structured, and at the same time, highly oscillatory near the wall, but our calculation method still converges exponentially fast and is capable to achieve an accuracy of 10^{-5} with $N = 300$ grid points. Note, however, that due to the highly oscillatory structure of the profile near the wall, the WDA might not be an appropriate approximation, and one should use a hard sphere part of the free energy functional, which is more sensitive to the correlation structure of the fluid, such as the FMT approximation.

When computing the interaction energy with Eq. (33), we need to verify that the length of the computational domain L is sufficient for the density to converge towards its asymptotic tail given by Eq. (30). This is mostly because the pseudospectral collocation methods are notoriously sensitive to discontinuities in the underlying solution,[45] and one needs to check *a posteriori* that the value initially chosen for L suffices for this convergence, so that the discontinuity introduced due to the finiteness of the computational domain is negligible. The typical value of L which we use for the calculation of the wetting isotherms was chosen to be approximately 2 times larger than the position of the liquid-vapor interface of the thickest

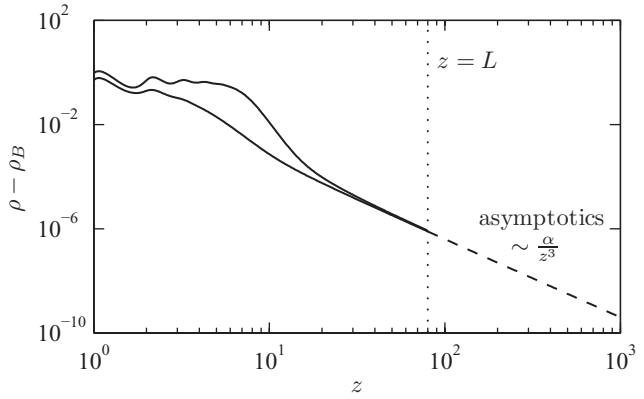

FIG. 2. Plots of $(\rho(z) - \rho_B)$ as a function of z, demonstrating the convergence of the density profile to its asymptotic tail, Eq. (30), for $N = 250$. The solid lines correspond to the coexisting density profiles from Fig. 1, whereas the dashed line comes from the asymptotic analysis, Eq. (30), with $\alpha \approx 0.4$. The dotted line demarcates the end of the computational domain at $z = L = 80$, where $\rho(L) - (\rho_B + \alpha/L^3) = O(10^{-7})$.

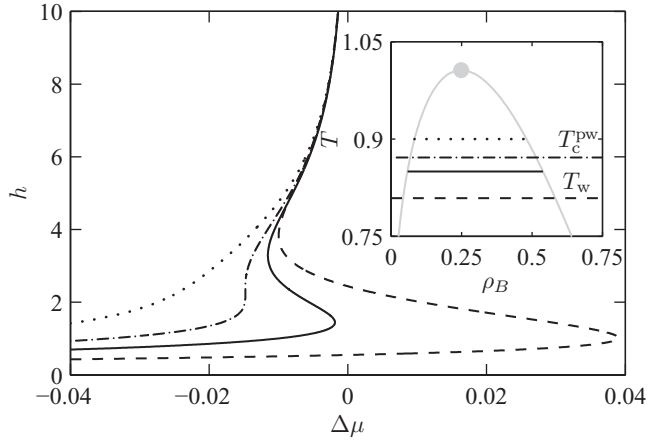

FIG. 3. Wetting isotherms calculated using WDA, with $E_w = 9.82$. The solid line shows an example of a prewetting transition at $T = 0.85$, $\Delta\mu_0 = -0.008$ followed by complete wetting at $\Delta\mu = 0$. Dashed and dotted-dashed lines demarcate the limiting cases for the occurrence of prewetting transitions, at $T_w = 0.81$, $\Delta\mu_0 = 0$ and $T_c^{pw} = 0.87$, $\Delta\mu_0 = -0.015$, respectively. The dotted line, for $T = 0.9$, corresponds to an example where complete wetting can occur without prewetting. The inset shows the corresponding values of temperatures on the coexistence phase diagram; a prewetting transition occurs in the range of temperatures $T_w \le T \le T_c^{pw}$.

profile we considered for a given isotherm. Figure 2 shows the asymptotic behavior of the two coexisting density profiles from Fig. 1(a), which are the typical profiles examined in the present study. It is evident from the figure that a domain of length $L = 80$ is sufficiently large for the density profile $\rho(z)$ to reach the characteristic cubic decay towards the bulk density, ρ_B. At the end of our computational domain, $z = L$, the difference between the calculated profile and its asymptotic tail given in Eq. (30) is found to be $O(10^{-7})$.

In adsorption problems, a characteristic measurable property to be considered is the coverage of the wall with a liquid film of thickness h, commonly considered as a function of the disjoining chemical potential, $\Delta\mu = \mu - \mu_{sat}$, where μ is the chemical potential of the fluid in contact with the wall, and μ_{sat} is the saturation chemical potential, i.e., the chemical potential corresponding to the coexistence of bulk liquid and bulk gas phases. The thickness of the film is given by $h = \Gamma/\rho_{liq}$, where ρ_{liq} is the density of the coexisting liquid and Γ is the adsorption. For the given potential of the substrate wall $V_{ext}(\mathbf{r})$ and the surface excess grand potential $\Omega^{ex}(\mu, T; V_{ext}(\mathbf{r}))$ per unit area, the adsorption is uniquely defined through the Gibbs relation, $\Gamma = -(\partial\Omega^{ex}/\partial\mu)_T$. Thus, for a planar wall with a z-dependent potential $V_{ext}(\mathbf{r}) \equiv V_{ext}(z)$, Γ is related to the density profile $\rho(z)$ by

$$\Gamma(\mu, T) = \int_0^\infty (\rho(z) - \rho_B)\, dz, \tag{45}$$

where, like before, ρ_B is the density of the gas in the bulk of the fluid, far from the wall.

Typically, for temperatures below the fluid's critical point and bulk densities below coexistence, several distinct types of surface phase transitions can be identified,[13,16,17,36] each corresponding to a particular topology of the wetting isotherm, the $\Delta\mu$ vs Γ curve at a constant temperature. For a hysteresis-type wetting isotherm, which possess turning points, or spinodals, it is possible to find multiple solutions to the equilibrium Eq. (27). For those cases the number of Newton's iterations required to converge to a solution is strongly dependent on the initial guess used to start the iteration algorithm and its proximity to one of the solutions; a "bad" initial guess may result in many Newton's iterations or in no convergence at all, which may happen in the vicinity of the spinodal point. Therefore, to trace all possible states as $\Delta\mu$ is varied, we employ a numerical technique known as pseudo-arclength continuation.[76] The technical details of this method, which are similar to the one presented by Frink and Salinger in Ref. 31, are given in the Appendix. The main idea is to treat the (independent) parameter μ as an unknown, closing the system of nonlinear algebraic equations with an additional geometric constraint. This allows to determine consistently all possible states, without relying on one's physical insight to come up with a good initial guess, as was done, for example, in some of the earlier studies (e.g., Refs. 28, 72, and 77).

Figure 3 shows the possible wetting scenarios of a fluid whose bulk density is below the liquid-vapor coexistence. The representative adsorption isotherms are plotted as functions of the disjoining chemical potential, $\Delta\mu$. The inset shows the bulk coexistence curve with the critical temperatures for the occurrence of the prewetting transition. For temperatures below the wetting temperature T_w, the observed equilibrium coverage h does not exceed several molecular diameters, even for bulk pressures approaching that of the saturated vapor. Such a scenario is referred to in the literature as partial wetting.[17] At the critical temperature $T = T_w$ the Maxwell equal area construction[36] becomes possible at $\Delta\mu = 0$, which means that a microscopic film can coexist with an infinitely thick film (see the dashed curve in Fig. 3).

For temperatures $T_w < T < T_c^{pw}$, a thin and thick microscopic films can coexist (see full curve in Fig. 3). It is manifested by the phenomenon of prewetting, whereby the coverage changes discontinuously when the disjoining chemical potential crosses the value $\Delta\mu_0$ obtainable from the Maxwell construction. In Sec. VIII, we show how the density profiles

corresponding to the different branches of such hysteresis-type isotherms have different stability characteristics as stationary solutions of the dynamic Eq. (28). As $T \to T_c^{pw}$ from below, the area given by the Maxwell construction at $\Delta\mu_0(T)$ vanishes (see the dashed-dotted curve in Fig. 3). For temperatures above T_c^{pw}, the observed coverage by film grows smoothly and continuously with $\Delta\mu$ as the fluid completely wets the substrate (the dotted curve in Fig. 3).

For strongly attractive substrates, the density profiles have pronounced oscillations in the near-wall region, and, with an increase in bulk pressure, such oscillations grow in amplitude, contributing to the value of adsorption. For even more strongly attractive substrates, the fluid can form a highly structured solid-like, rather than liquid-like, film in the immediate vicinity of the wall and the wetting isotherms become stair-like. In that case, as $\Delta\mu \to 0$ the fluid undergoes a succession of first-order wetting transitions similar to the prewetting transition described above. Each first-order wetting transition has its own range of temperatures where a jump in coverage occurs. Such wetting scenario is referred to as layering transition.[36,72,74]

Finally, we contrast the WDA prescription for the reference hard sphere functional with LDA and FMT. As noted in Sec. II, LDA can be classified as the simplest model for the hard sphere fluid which can account for the spatial dependence of the number density. Within LDA, the configurational part of the free energy in Eq. (10) is evaluated directly at the density $\rho(\mathbf{r})$. In the early literature, models based on LDA were quite popular.[55,78,79] The analysis of the structure factor suggests that only the liquid-vapor interface can be described adequately by LDA, provided that the wall effects can be neglected.[55,79] Despite this limitation, LDA is still employed to date in qualitative descriptions of adsorption, mainly due to its computational simplicity, e.g., Refs. 59 and 80.

The version of WDA used for the free energy entering Eq. (28) can in turn be classified as the simplest model which can account not only for the spatial dependence of the fluid number density but also for the excluded volume correlations within the hard sphere fluid.[52,79] In fact, WDA can be viewed as a generalization of LDA, since the latter can be retrieved with the weight function $W_{\mathrm{LDA}}(\mathbf{r}) \equiv \delta(\mathbf{r})$ in Eqs. (9) and (10). As noted in Sec. II, WDA approximations are constructed by selecting a prescription for the weighting function in Eq. (9) in such a way that the resulting hard sphere functional reproduces the known correlation structure of the bulk fluid via the functional differentiation route.[25,53] A systematic comparative study of various WDA prescriptions for the hard sphere functional in problems of liquid adsorption can be found in Refs. 6 and 28.

More sophisticated approximations for the hard sphere part of the fluid's free energy belong to the FMT family. As also noted in Sec. II, the FMT methodology is based on constructing a functional which would reduce to exactly known results in the limiting cases of zero density and constant bulk density.[61,62] An alternative route is known as dimensional reduction, where the hard sphere functional is constructed to reproduce exactly the zero-dimensional limit.[81] The distinct feature of the FMT family of approximations is that the hard sphere functional is constructed as a local function of the fundamental measures, Eqs. (12)–(15), which are themselves non-local weighted averages of the density. Such choice of variables is dictated by the geometric qualities of non-penetrable hard bodies and is invariant with respect to the dimensionality of the fluid and even the shape of its constituent molecules. There exist FMT approximations for fluids and fluid mixtures consisting of non-spherical hard molecules.[48] With an FMT approximation the correlation structure of the hard sphere fluid can be obtained as output from the theory and usually compares very well with simulation results. A detailed analysis of various FMT prescriptions can be found in Refs. 29, 48, and 82.

Unfortunately, the technical difficulties involved in the practical implementation of FMT functionals, where it is necessary to compute several fundamental measures (see Eqs. (15)), force some authors to use simpler approximations like WDA or even LDA, especially when dealing with higher-dimensional problems, see, e.g., Ref. 59. We expect, however, that the use of the numerical methodology developed here would facilitate the calculation process. As an illustration, we have calculated the prewetting lines for various values of the substrate parameter E_w using the White Bear FMT (Ref. 62) in the hard sphere part of the free energy functional. The calculation of a prewetting line is equivalent to the calculation of a set of prewetting isotherms for varying values of T, which is straightforward using the continuation algorithm (see the Appendix). Moreover, the algorithm can, in principle, be nested to allow for consecutive continuation of solutions to Eq. (27) over several parameters (μ and T in that case). Therefore, such a scheme constitutes a systematic tool for calculating prewetting lines, as well as other kinds of phase diagrams.

Figure 4 shows a sequence of prewetting lines together with their spinodals plotted in the $T - \Delta\mu$ plane, each corresponding to a different value of the substrate parameter, E_w, see Eqs. (16) and (17). Given E_w, each prewetting line is defined for $T_w < T < T_c^{pw}$ and, together with its spinodals, it divides the $T - \Delta\mu$ half-plane ($\Delta\mu < 0$) into regions corresponding to the thermodynamic stability of films of various

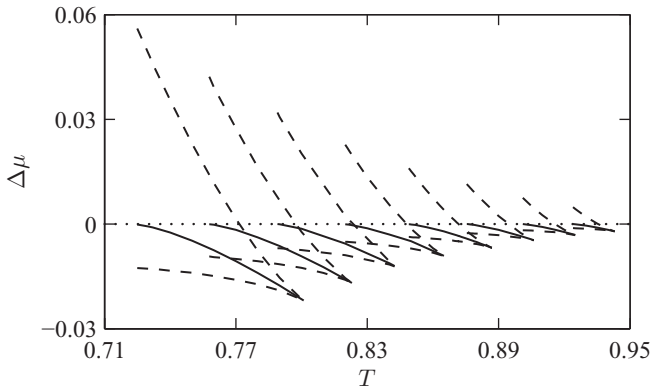

FIG. 4. Prewetting lines (full line) with spinodals (dashed line) for several values of E_w, decreasing from right to left, calculated using FMT. For fixed E_w, points on each prewetting line form the locus of $(\Delta\mu_0, T)$, and points on its spinodals form the locus of the turning points of their respective isotherms. The parameter E_w takes the values (right to left): 11.78, 11.29, 10.80, 10.31, 9.82, 9.33, 8.84, 8.35.

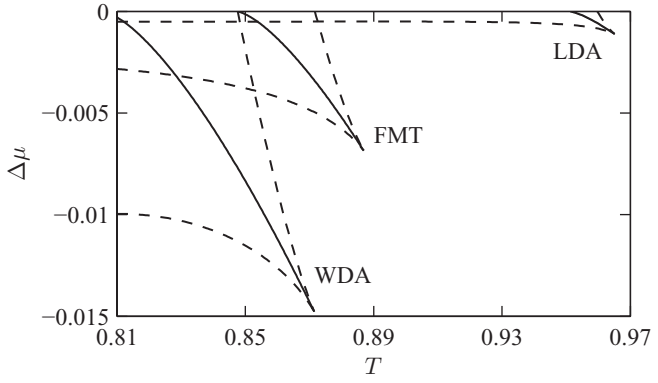

FIG. 5. Prewetting lines (full line) with spinodals (dashed line) for $E_w = 9.8$ calculated using (left to right) WDA, FMT, and LDA.

thicknesses. As the strength of the substrate potential is decreased, the prewetting lines shift towards the critical temperature of the fluid and the range of temperatures $T_w < T < T_c^{pw}$ shrinks. For values of E_w larger than those shown in Fig. 4, the isotherms tend to become stair-like, which is typical of the layering transition (for more details consider, e.g., Refs. 13, 16, 36, 72, and 74).

For a given strength of the substrate potential, DFTs using different approximations for the hard sphere part of the free energy functional normally predict markedly different wetting behavior, as can be seen in Fig. 5, which shows the prewetting lines calculated using LDA, WDA and FMT. A direct comparison between the density profiles obtained from WDA and FMT makes sense for temperatures exceeding the T_c^{pw} obtained from the two DFTs. A comparison between WDA and the White Bear FMT approximation is given in Fig. 6 for the case where both predict complete wetting. As can be seen, WDA possesses a qualitative agreement with a more sophisticated FMT approximation for both the liquid-vapor interface and the near-wall structure of the profile, for values of μ relatively close (e.g., Fig. 6(a)) and relatively far (e.g., Fig. 6(c)) from coexistence. The reason for the agreement in the case of complete wetting is, of course, the fact that for high values of temperature the profiles are not very structured near the wall, and WDA turns out to be a sufficiently good approximation. The density profiles calculated in a region of the disjoining chemical potential where the wetting isotherm bends, typically reveal a disagreement between the calculations using WDA and FMT (e.g., Fig. 6 (b)). As the value of T is increased further, the agreement between WDA and FMT would persist for larger intervals of μ, and the respective isotherms corresponding to either approximation would be "closer" to each other on the $\Delta\mu - h$ plane. On the other hand, for lower temperatures the effects of packing become more important, and the density profiles obtained using FMT and WDA differ significantly.

As previously mentioned, the liquid-vapor interfaces of the profiles obtained from different DFTs, even from LDA, can match as $\Delta\mu \to 0$, irrespective of the temperature. Figure 7 shows a calculation based on the WDA and the LDA prescriptions for the hard sphere functional, for the cases of partial wetting scenarios, i.e., the value of T is below the

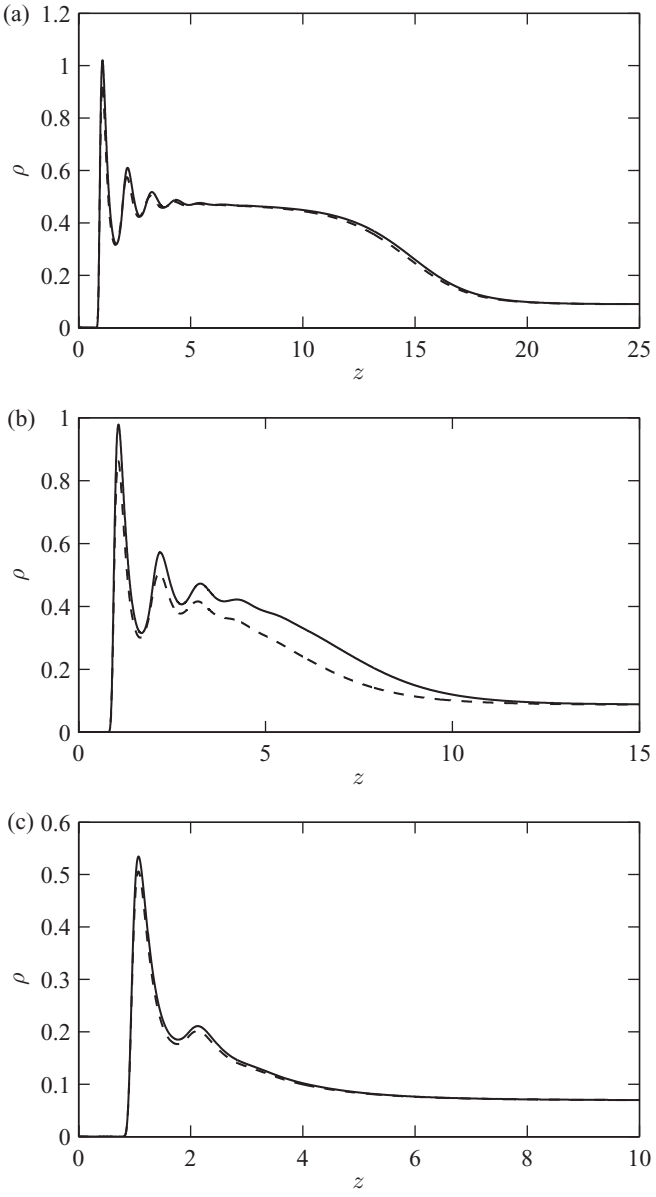

FIG. 6. Wetting profiles calculated using WDA (solid curves) and FMT (dashed curves), with $E_w = 9.82$, $T = 0.91$. (a) Thick adsorbed film, $\Delta\mu = -10^{-3}$; (b) thinner adsorbed film, $\Delta\mu = -10^{-2}$; and (c) no film is adsorbed, $\Delta\mu = -10^{-1}$.

T_w value predicted by both approximations. The liquid-vapor interfaces match for rather thick profiles as $\Delta\mu \to 0$ (see Fig. 7(a)). The liquid-vapor interface of such profiles is essentially free from the effects of the wall. For larger $\Delta\mu$, see Fig. 7(b), the effects of the near-wall layering alter the liquid-vapor interface of the profiles calculated using WDA as compared to that obtained from LDA. This result confirms the analysis made by other authors (e.g., Ref. 55), and illustrates the limited applicability of local DFTs.

VIII. DYNAMICS OF ADSORBED FILM

In this section we consider the relaxation dynamics of an adsorbed fluid as given by Eq. (28). A dynamic process can be triggered, for example, by switching off an initially present

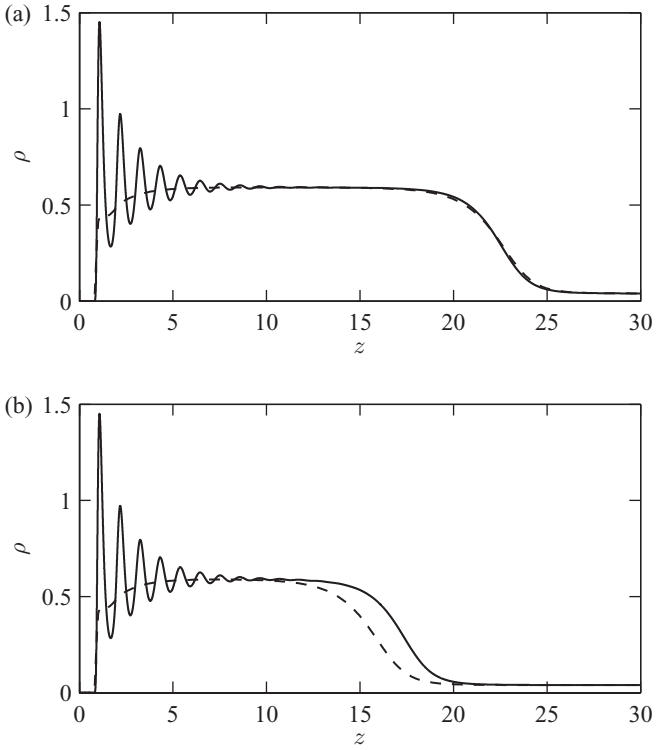

FIG. 7. Wetting profiles calculated using WDA (solid line) and LDA (dashed line), with $E_w = 9.82$, $T = 0.8$. (a) Thick adsorbed film, $\Delta\mu \approx -10^{-4}$ and (b) thin adsorbed film, $\Delta\mu \approx -10^{-3}$.

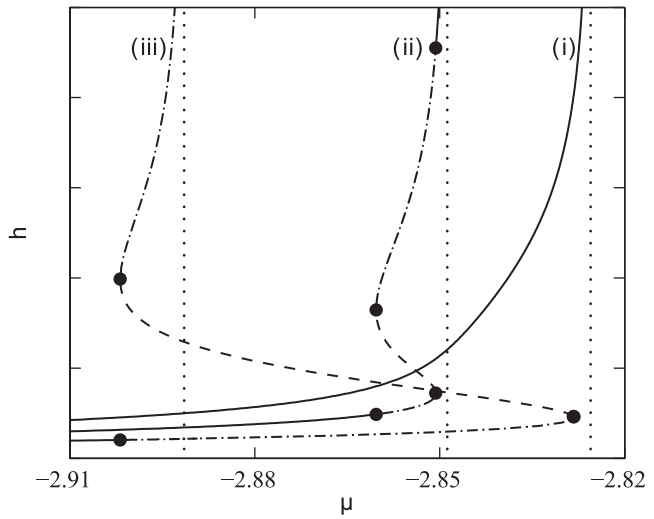

FIG. 8. Adsorption isotherms calculated using WDA, with $E_w = 9.82$. The solid, dashed-dotted, and dashed branches correspond to stable, metastable, and unstable stationary solutions of Eq. (28): (i) complete wetting at $T = 0.9 > T_c^{pw}$, (ii) prewetting at $T_w < T = 0.85 < T_c^{pw}$, and (iii) partial wetting scenario at $T = 0.79 < T_w$. The coexistence values of chemical potentials for each temperature are shown by the vertical asymptotes of the isotherms (demarcated by dotted lines). Filled circles are added for clarity to mark the points where the isotherm branches change stability.

external field. The dissipative second term in Eq. (28) ensures that the bulk value of the chemical potential remains equal to μ at all times, which, in turn, allows to visualize the evolution of the film thickness h conveniently in the $\Delta\mu - h$ plane.

Formulating the equation for the dynamics of the density distribution $\rho(z, t)$ allows for a stability analysis of the associated equilibrium profiles with respect to perturbations and an interpretation of the adsorption isotherms in terms of the dynamic stability of h. For example, in hysteresis-type isotherms, like those of prewetting or partial wetting scenarios, we can identify metastable, stable, and unstable branches in relation to Eq. (28). We also consider the relative effects of dissipative and conservative processes on the evolution of the system, which may exhibit either dynamic drying (decreasing film thickness $h(t)$) or wetting (increasing $h(t)$).

Figure 8 shows the dynamic stability of the three types of wetting isotherms described in Sec. VII. Every point on the isotherm corresponds to a density profile providing a stationary solution to Eq. (28). The characteristic of a stable branch is that when the associated density profiles are perturbed and allowed to relax, they will always return back to the respective unperturbed, stable stationary states. A density profile associated with a point on a metastable branch possesses a basin of attraction in the phase space of Eq. (28), where the value of μ is fixed, and only initial conditions $\rho(z, t = 0)$ within it eventually relax to the respective metastable state. In comparison, the basin of attraction of a stable density profile covers the whole phase space. An unstable state cannot be reached through a dynamic process, and hence cannot be observed. Any infinitesimal perturbation imposed on an unstable density profile will force it to evolve to a metastable equilibrium state. For a given value of the chemical potential the dynamic Eq. (28) can have a single stable stationary solution or up to two metastable ones, always accompanied by an unstable stationary solution.

The process of complete wetting (curve (i) in Fig. 8) gives rise to an entirely stable isotherm. Any hysteresis-type isotherm (curves (ii) and (iii)) possesses two metastable branches, with the lower metastable branch of a partial wetting isotherm extending above the coexistence value of chemical potential (curve (iii)).

In our numerical experiments we solved Eq. (28) imposing a vanishing flux at the wall and in the bulk of the fluid, enforced by requiring that

$$\frac{\partial}{\partial z}\frac{\delta F}{\delta \rho}\Big|_{z=0,\infty} = 0, \tag{46}$$

at all times. The far-field flux condition is more naturally applied when $L \to \infty$ in Eq. (36), which also eliminates the need for asymptotics to calculate the non-local terms in Eq. (25). For marching in time, we use the `ode15s` function in MATLAB™, which is based on an implicit scheme with backward differentiation formulas and adaptive time stepping.[83] For our calculations, we typically used 200–300 mesh points with a relative tolerance of 10^{-8} for each time step, which typically required less than 10 min on a standard 64-bit desktop computer.

To study the dynamics near the unstable branch of the isotherm, we constructed initial density profiles, $\rho(z, t = 0)$, by solving the equilibrium Eq. (27) with an additional small external field $\delta(z)$:

$$\frac{\delta F[\rho]}{\delta \rho} - \mu + \tilde{\delta}(z) = 0, \tag{47}$$

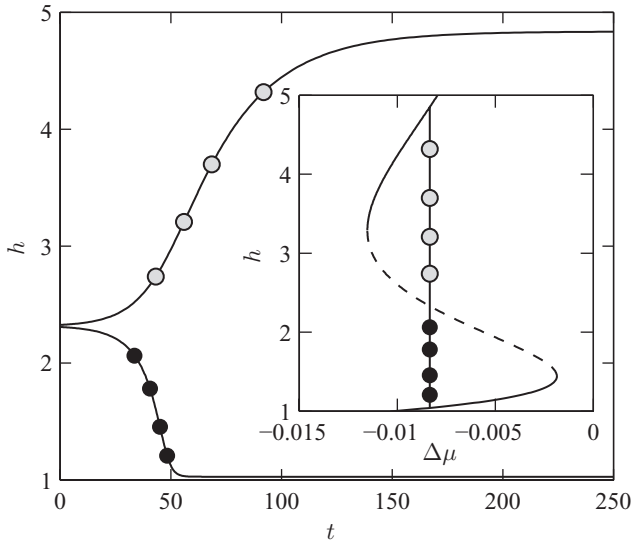

FIG. 9. Evolution of film thickness $h(t)$ corresponding to an unstable branch of a hysteresis-type isotherm, for $T = 0.85$, $\Delta\mu = -0.008$, $\kappa = 0.5$, $E_w = 9.82$. Perturbed unstable equilibrium states evolve to either of the two metastable states, depending on the sign of the small perturbation in Eq. (47). The filled black and gray circles correspond to the snapshots of the evolving density profiles shown in Figs. 10(a) and 10(b), respectively. The inset shows the position of time-dependent film thickness on the adsorption isotherm.

where $\tilde{\delta}(z)$ is an arbitrary, localized function with $|\tilde{\delta}(z)| \ll 1$ and $\tilde{\delta}(z) \to 0$ as $z \to \infty$. Equation (47) allows us to obtain density profiles that are arbitrarily close to an equilibrium profile associated with a point on the unstable branch.

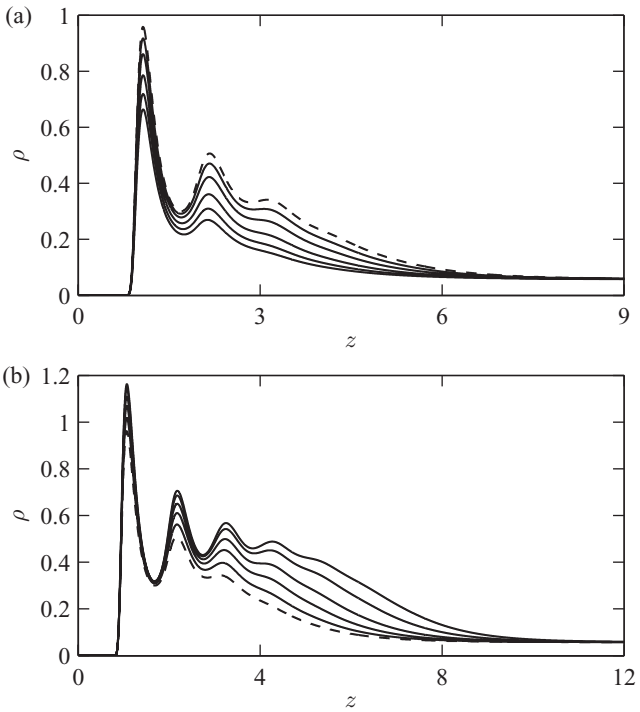

FIG. 10. Snapshots of evolving unstable density profiles relaxing to respective metastable states; for the parameters see Fig. 9. Dashed curves correspond to the initial density distributions, obtained by imposing a small perturbation to an unstable profile. (a) Drying process (from top to bottom) at times $t = 33, 40, 45$, and 48. (b) Wetting process (from bottom to top) at times $t = 43, 56, 69$, and 91.

When the system relaxes to equilibrium, the evolution is dependent on the sign of the disturbance in Eq. (47) (see Fig. 9). The initial profiles with $\tilde{\delta}(z) > 0$ evolve to thicker profiles, whereas those with $\tilde{\delta}(z) < 0$ evolve to the thinner profiles. In the phase space of stationary solutions of dynamic Eq. (28), such conditions for $\tilde{\delta}(z)$ correspond to a small perturbation of the unstable profile in the direction of either of the metastable equilibrium states. We also observe that the drying process requires less time than the wetting one, which here may be attributed to the initial proximity of the unstable profile to the lower metastable branch of the isotherm (see, for example, the inset of Fig. 9). Figure 10 depicts a few selected snapshots of the relaxing density profiles.

Next, consider the relaxation of the liquid film from a large, possibly macroscopic, thickness to a much lower, microscopic one. Such a dynamic process of drying can be triggered by instantly changing the temperature or pressure of a fluid near coexistence to favor a much thinner adsorbed film. For these configurations, the initial density profile can be formed by choosing an equilibrium profile at a different μ from that of the dynamic problem but making sure that the profile asymptotically approaches the bulk density of the dynamic problem. Several representative examples of temporal evolution of the liquid film are presented in Fig. 11 together

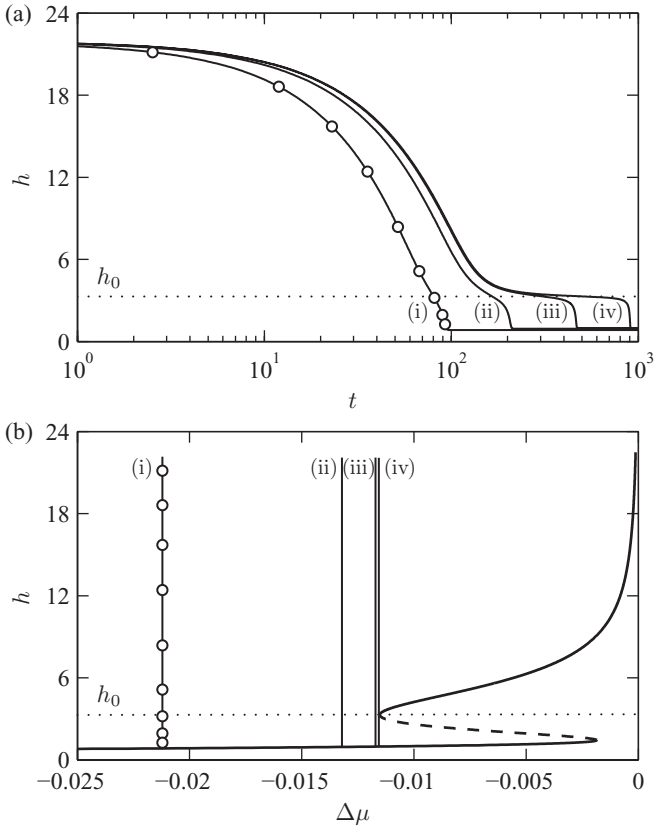

FIG. 11. Dynamical drying of thick films, $T = 0.85$, $E_w = 9.82$, and $\kappa = 1$. The values of disjoining chemical potential are $\Delta\mu = -0.021, -0.013, -0.0117$, and -0.0116 for curves (i)–(iv), respectively. (a) Temporal evolution of film thickness $h(t)$ and (b) position of curves (i)–(iv) on the adsorption isotherm. Open circles correspond to the snapshots of evolving density profiles in Fig. 12. As $\Delta\mu$ approaches the left spinodal of the isotherm, the evolution of the film thickness $h(t)$ slows down near the value $h_0 = 3.3$ at the spinodal point.

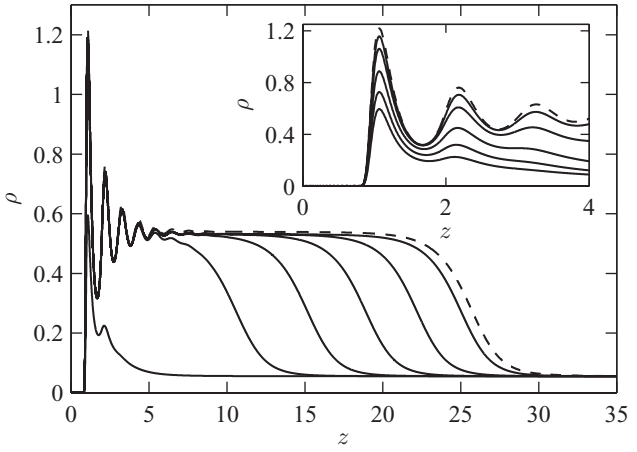

FIG. 12. Snapshots of evolving density profile in a drying process (see curve (i) in Fig. 11). The dashed line corresponds to the initial density profile, whereas the solid lines show the density profiles (from right to left) at intermediate times $t = 2.5, 12, 23, 35.5$, and 52, which is continued on the inset zooming into the near-wall region, at times $t = 52, 67, 81, 89.5$, and 92.5. The evolution of the fluid-wall interface begins much later, after the liquid-vapor interface starts to recede, at $t > 52$.

with a selection of snapshots of the density profiles at different times, as shown in Fig. 12.

When we choose μ to be closer to the spinodal point of the isotherm, the film thickness takes more time to equilibrate (see curves (i)–(iv) in Fig. 11(a)), exhibiting in the extreme case a nearly steady behavior when the height of the film reaches that of the spinodal point, h_0 (see, e.g., curve (iv) in Fig. 11(a)). This behavior is a dynamic manifestation of the presence of hysteresis in the equilibrium isotherm. In principle, it is possible to choose a chemical potential so that the film thickness would stay in the vicinity of h_0 for any given finite period of time, but as $t \to \infty$, the film would eventually relax to the stationary value on the isotherm (see Fig. 12 for an example of evolving density profiles).

The attraction to stable (or metastable) solutions becomes rather extreme during dynamic wetting, when the system is near total saturation and $\Delta\mu \to 0^-$. Similarly to the previously considered case of drying, we can trigger a relaxation process by, e.g., instantaneously changing the temperature and the bulk pressure of an equilibrium fluid which partially wets the substrate. In the resulting dynamic process of wetting the system appears to be attracted not just to a single stable solution, like in the above case of drying near a spinodal point, but to the whole set of stable equilibrium solutions with similar values of μ. Depending on the proximity of the chemical potential to coexistence, the evolution to the final state can take arbitrarily long times, as shown in Fig. 13. On the other hand, for intermediate values of μ, that are sufficiently far from both the spinodal and saturation points, relaxation occurs over the shortest period of time (see, e.g., curves corresponding to the evolution towards h_2 in Fig. 13).

Finally, we consider the relative effect of conservative and dissipative processes of Eq. (28) due to the parameter κ. Since the system equilibrates, in theory, in an infinite amount of time, to analyze the effect of κ, we have to introduce an "equilibration time" t_{eq}, which we define as the time required

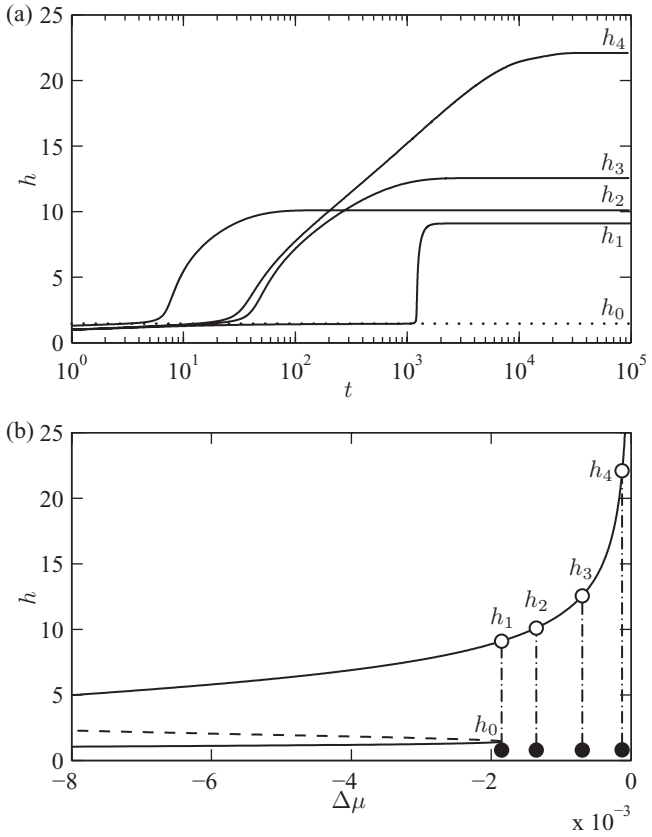

FIG. 13. Relaxation of film thickness to a larger value, $E_w = 9.82$, $T = 0.85$, $\kappa = 1$. Filled and open circles denote the initial and final thicknesses for each dynamic process, respectively. The final thicknesses h_1–h_4 correspond to $\Delta\mu = -0.00185, -0.00135, -0.00012$, and -0.0007, respectively. (a) Temporal evolution of film thickness $h(t)$ and (b) position of time-dependent film thickness on the adsorption isotherm. The process of evolution to h_1 is slowed down by the presence of the spinodal point with $h_0 = 3.3$. At $\Delta\mu = -0.0007$ the process of evolution to h_4 is rather slow due to its proximity to saturation.

for the adsorbed film to achieve 90% of its equilibrium thickness. Our computations reveal that for all processes considered t_{eq} is inversely proportional to κ, with the coefficient of proportionality depending on the initial condition (see, for example, Fig. 14 for a representative computation).

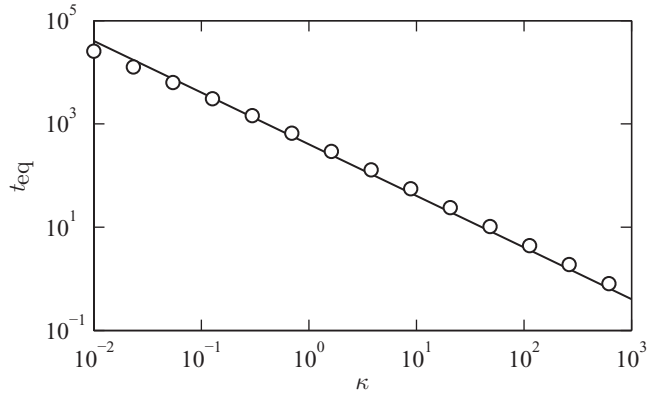

FIG. 14. The effect of relative rate parameter κ, Eq. (28), on the equilibration time, t_{eq}, for processes following the evolution of curve (iii) in Fig. 11(b). The plot shows the computed (open circles) t_{eq} as a function of κ, together with the least squares fit, $t_{eq} = 403/\kappa$ (solid line).

IX. CONCLUSION

We have developed a novel numerical scheme for solving the typical integral equations of DFT and integro-differential equations of DDFT. One of the main features of this type of equations is the presence of one or more non-local integral terms resulting from the attractive intermolecular interactions and/or from the coarse-graining of density associated with repulsive interactions. Our numerical methodology is based on the Chebyshev rational pseudo spectral collocation scheme and uses a global interpolating function to represent the solution on the entire computational domain. Mathematical operations like differentiation and integration are implicitly performed on the global interpolant by acting linearly on the discrete data. The discretization points can be concentrated in regions where the solution exhibits rapid variations, while moderate number of grid points may be kept in the areas where the solution varies slowly. The method converges exponentially as the number of discretization points increases and also allows us to incorporate the asymptotic behavior of the solution. Coupling of our discretization scheme with a continuation algorithm allows to compute accurately and efficiently complete phase diagrams.

For the equilibrium problem we have used three different approximations for the hard sphere part of the free energy functional, namely LDA, WDA and FMT. We have provided a detailed comparison between the results obtained from these theories and indicated the range of parameters like temperature and chemical potential where they give similar results. Any alternative formalisms can be readily implemented by applying the same concepts and ideas we developed for the prototypical models considered in the present study.

We have adapted the well-known equations for the subcritical dynamic behavior of DFT models to the problem of wetting/drying and have shown that the wetting isotherms can be interpreted in terms of stability of the corresponding equilibria. In the case of complete wetting all the equilibrium solutions are dynamically stable, and a perturbed profile would always return to the equilibrium state corresponding to the same bulk density. In the cases where the wetting isotherm has a hysteresis-type behavior, one can distinguish branches of different stability. Depending on the initial proximity of the density distribution to either of the metastable solutions in the phase space of the dynamic equation, the evolution can develop through either dynamic wetting or drying towards thicker or thinner films, respectively. The evolution of the substrate coverage maintains a nearly stationary behavior in the vicinity of the isotherm's spinodal points for long but finite times. Such dynamic behavior of the liquid film is a manifestation of hysteresis in the equilibrium wetting isotherm.

When the chemical potential of a system with microscopically small coverage is shifted to a value slightly below that of the coexisting liquid and vapor, the resulting dynamic coverage becomes increasingly slow as the chemical potential approaches coexistence making the time-dependent density profile appear to be attracted to the equilibrium profiles with similar values of μ. In reality, however, since μ is fixed in the dynamic equation, these nearby equilibria do not exist.

While the present study focused specifically to the problem of a liquid film adsorbed at a planar wall, our methodology is general and can be applied to virtually any DFT problem in 1D. More importantly, the characteristic accuracy and efficiency of our scheme clearly demonstrated its superiority over the conventional schemes, thus making its extension to 2D configurations rather appealing (e.g. topographical substrates which are known to affect the wetting properties substantially[84–86]). This extension and related problems will be examined in a future study.

ACKNOWLEDGMENTS

We are grateful to the anonymous referee for helpful comments and suggestions. This work is supported by European Union-FP7 ITN Grant No. 214919 (Multiflow) and European Research Council Advanced Grant No. 247031.

APPENDIX: NUMERICAL CONTINUATION

Here we describe the numerical technique used for obtaining a set of solutions to continuation problems with a free parameter. The mathematical details of the methodology can be found in Refs. 76 and 87, while its practical aspects are described in Ref. 88 within the context of dynamical systems. The technique is general, in the sense that it is applicable to any set of discretized equations. It is important to note that the notation hereby used is independent of the notation of the other quantities used throughout the paper.

A problem with one free parameter which is discretized with an N-point scheme can be written in the form, $\mathbf{F}(\mathbf{x}) = \mathbf{0}$. Here $\mathbf{F} : \mathbb{R}^{N+1} \to \mathbb{R}^N$ represents the discretized equation and the elements of $\mathbf{x} \in \mathbb{R}^{N+1}$, $\mathbf{x} = [\mathbf{y}, \mu]$, contain the discretized solution $\mathbf{y} \in \mathbb{R}^N$ as well as the corresponding value of the bifurcation parameter, μ. Given a starting point $\mathbf{x}_0$ in this $(N+1)$-dimensional space, so that $\mathbf{F}(\mathbf{x}_0) = \mathbf{0}$, we would like to numerically continue that solution along the values of the parameter, μ, by essentially treating it as an unknown, thus obtaining the bifurcation branches of the solution as a function of μ. Hence, the N-dimensional vector-function $\mathbf{F}(\mathbf{x}) \equiv [F_1(\mathbf{x}), \ldots, F_N(\mathbf{x})]$ must be supplemented with an additional component $F_{N+1}(\mathbf{x})$, so that $[F_1(\mathbf{x}), \ldots, F_{N+1}(\mathbf{x})] = \mathbf{0}$ forms a set of $N+1$ equations for the same number of unknowns.

To show how the additional constraint can be obtained, the problem is considered in geometric terms. In $\mathbb{R}^{N+1}$, the locus of the N intersecting hypersurfaces given by the components of $\mathbf{F}(\mathbf{x}) = \mathbf{0}$ is a $(N+1)$-dimensional space curve. Thus, given a starting point $\mathbf{x}_0 \equiv [\mathbf{y}_0, \mu_0]$, we seek to parametrize that curve in the form $\mathbf{x}(l)$, or, equivalently, to find a systematic way to obtain its points in $\mathbb{R}^{N+1}$. (Note that when the parameter μ is fixed at its initial value μ_0, the equation $\mathbf{F}(\mathbf{y}, \mu_0) = \mathbf{0}$ can be viewed as the intersection of N hypersurfaces in $\mathbb{R}^N$, its locus being a single point—the solution $\mathbf{y} \in \mathbb{R}^N$.)

The vector $\boldsymbol{\tau}_0$ tangent to the curve $\mathbf{x}(l)$ at point $\mathbf{x}_0$ spans the null-space of the Jacobian matrix of dimensions $N \times (N+1)$ evaluated at point $\mathbf{x}_0$, $F_x(\mathbf{x}_0) = \partial \mathbf{F}/\partial \mathbf{x}|_{\mathbf{x}_0}$. To obtain the next point on the curve $\mathbf{x}(l)$ we use a predictor-corrector scheme, where we first displace the starting point by distance

ds along the tangent for a predictor step:

$$\mathbf{X}^0 = \mathbf{x}_0 + ds\,\boldsymbol{\tau}_0. \tag{A1}$$

For the corrector step, we apply Newton's method to the following set of $N+1$ equations to solve for $\mathbf{x}$:

$$\mathbf{F}(\mathbf{x}) = \mathbf{0}, \tag{A2a}$$

$$F_{N+1}(\mathbf{x}) \equiv \left(\mathbf{x} - \mathbf{X}^0\right) \cdot \boldsymbol{\tau}^* = 0, \tag{A2b}$$

where the dot denotes the inner product and star denotes transpose. The number of ith Newton's iteration, which produces the vector $\mathbf{X}^i$ is in the superscript.

The above equations correspond to the geometric problem in $\mathbb{R}^{N+1}$ of finding the intersection of the curve defined by N intersecting hypersurfaces: $\mathbf{F}(\mathbf{x}) = 0$, and the hyperplane defined by its normal vector $\boldsymbol{\tau}$ and the point $\mathbf{X}^0$.

The choice $\boldsymbol{\tau} = \boldsymbol{\tau}_0$ in Eq. (A2b), followed by Newton's iterations to find $\mathbf{x}$ corresponds to Keller's continuation method.[76] After the next point $\mathbf{x} = \mathbf{x}_1$ on the curve is found, the new tangent vector $\boldsymbol{\tau}_1$ is the vector spanning the null space of $F_x(\mathbf{x}_1)$. Keller's continuation scheme was employed e.g. in the recent study by Nold *et al.*[80] on wetting of a curved substrate.

In this study we employ a slightly different method, developed originally for systems of differential equations, the so-called Moore-Penrose algorithm,[88] where we define $\boldsymbol{\tau}$ in Eq. (A2b) as the tangent vector to the curve $\mathbf{x}(l)$ at point $\mathbf{x}$. Geometrically this choice of $\boldsymbol{\tau}$ corresponds to the requirement that $\mathbf{x}$ is the point on the curve $\mathbf{x}(l)$ which is closest to $\mathbf{X}^0$. Unlike Keller's scheme, we have to solve simultaneously for $\boldsymbol{\tau}$ as well as $\mathbf{x}$, but this extra work is comparable to the work required to find the null space of Jacobian in Keller's method. The advantage, however, is that the estimate we obtain for $\boldsymbol{\tau}$ is expected to be slightly more accurate. The convergence of both methods is schematically illustrated in Fig. 15, which shows the point $\mathbf{x}_{i+1}$ being obtained from the point $\mathbf{x}_i$.

We conclude the Appendix, by providing the Newton's algorithm for solving Eqs. (A2) for $\{\mathbf{x}, \boldsymbol{\tau}\}$, starting with $\{\mathbf{X}^0, \mathbf{T}^0\}$, and iterating over $\{\mathbf{X}^k, \mathbf{T}^k\}$ until the norm of the right-hand side of Eqs. (A2) becomes less than some required tolerance:[88]

$$\mathbf{X}^{k+1} = \mathbf{X}^k - H_{\mathbf{x}}^{-1}(\mathbf{X}^k, \mathbf{T}^k) H(\mathbf{X}^k, \mathbf{T}^k), \tag{A3}$$

$$\mathbf{T}^{k+1} = \mathbf{T}^k - H_{\mathbf{x}}^{-1}(\mathbf{X}^k, \mathbf{T}^k) R(\mathbf{X}^k, \mathbf{T}^k), \tag{A4}$$

where

$$H(\mathbf{X}, \mathbf{V}) = \begin{pmatrix} F(\mathbf{X}) \\ 0 \end{pmatrix}, \tag{A5}$$

$$H_{\mathbf{x}}(\mathbf{X}, \mathbf{T}) = \begin{pmatrix} F_{\mathbf{x}}(\mathbf{X}) \\ \mathbf{T}^* \end{pmatrix}, \tag{A6}$$

$$R(\mathbf{X}, \mathbf{T}) = \begin{pmatrix} F_{\mathbf{x}}(\mathbf{X})\,\mathbf{T} \\ 0 \end{pmatrix}. \tag{A7}$$

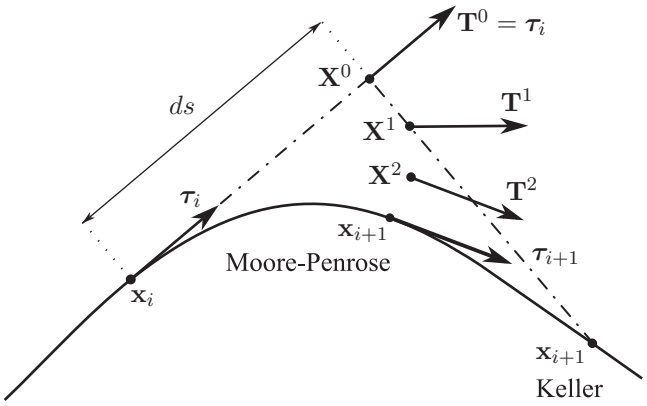

FIG. 15. Moore-Penrose and Keller continuation algorithms.

[1] R. Roth and A. O. Parry, Mol. Phys. **109**, 1159 (2011).
[2] C. Rascon and A. O. Parry, Nature (London) **407**, 986 (2000).
[3] A. Sartori and A. O. Parry, J. Phys.: Condens. Matter **14**, L679 (2002).
[4] L. J. D. Frink and A. G. Salinger, J. Chem. Phys. **118**, 7466 (2003).
[5] L. Szybisz and S. A. Sartarelli, J. Chem. Phys. **128**, 124702 (2008).
[6] T. Vanderlick, L. E. Scriven, and H. T. Davis, J. Chem. Phys. **90**, 2422 (1989).
[7] R. Evans, J. Phys.: Condens. Matter **2**, 8989 (1990).
[8] E. Ruckenstein and G. O. Berim, Advances in Colloid and Interface Science **154**, 56 (2010).
[9] P. De Gennes, Rev. Mod. Phys. **57**, 827 (1985).
[10] E. Ruckenstein and G. O. Berim, Adv. Colloid Interface Sci. **157**, 1 (2010).
[11] J. W. Cahn, J. Chem. Phys. **66**, 3667 (1977).
[12] C. Ebner and W. F. Saam, Phys. Rev. Lett. **38**, 1486 (1977).
[13] C. Domb and J. Lebowitz, *Phase Transitions and Critical Phenomena* (Academic, 1988), Vol. 12.
[14] R. Evans, Adv. Phys. **28**, 143 (1979).
[15] H. Lowen, J. Phys.: Condens. Matter **14**, 11897 (2002).
[16] R. Evans and A. Parry, J. Phys.: Condens. Matter **2**, SA 15 (1990).
[17] D. Bonn and D. Ross, Rep. Prog. Phys. **64**, 1085 (2001).
[18] P. J. Marshall, M. M. Szczęśniak, J. Sadlej, G. Chałasiński, M. A. ter Horst, and C. J. Jameson, J. Chem. Phys. **104**, 1996 (1996).
[19] A. Chizmeshya, M. W. Cole, and Z. Zaremba, J. Low Temp. Phys. **110**, 677 (1998).
[20] F. Ancilotto and F. Toigo, Phys. Rev. B **60**, 9019 (1999).
[21] G. Mistura, F. Ancilotto, L. Bruschi, and F. Toigo, Phys. Rev. Lett. **82**, 795 (1999).
[22] Y. Fan and P. Monson, J. Chem. Phys. **99**, 6897 (1993).
[23] Y. Yu, Y. Li, and Y. Zheng, Chin. Phys. Lett. **27**, 037101 (2010).
[24] E. Velasco and P. Tarazona, J. Chem. Phys. **91**, 7916 (1989).
[25] M. B. Sweatman, Phys. Rev. E **63**, 031102 (2001).
[26] S. A. Sartarelli and L. Szybisz, Phys. Rev. E **80**, 052602 (2009).
[27] Y.-X. Yu, J. Chem. Phys. **131**, 024704 (2009).
[28] S. Dhawan, M. E. Reimel, L. E. Scriven, and H. T. Davis, J. Chem. Phys. **94**, 4479 (1991).
[29] R. Roth, J. Phys.: Condens. Matter **22**, 063102 (2010).
[30] J. P. Noworyta, D. Henderson, S. Sokolowsky, and K.-Y. Chan, Mol. Phys. **95**, 415 (1998).
[31] A. G. Salinger and L. J. D. Frink, J. Chem. Phys. **118**, 7457 (2003).
[32] T. Laurila, M. Pradas, A. Hernández-Machado, and T. Ala-Nissila, Phys. Rev. E **78**, 031603 (2008).
[33] L. Pismen, Phys. Rev. E **64**, 021603 (2001).
[34] P. Hohenberg and B. I. Halperin, Rev. Mod. Phys. **49**, 435 (1977).
[35] J. S. Langer, *Solids Far from Equilibrium* (Cambridge University Press, Cambridge, 1992), Chap. 3, pp. 297–363.
[36] R. Evans, "Density functionals on the theory of nonuniform fluids," in *Fundamentals of Inhomogeneous Fluids* (Dekker, New York, 1992), p. 85.
[37] T. Munakata, Aust. J. Phys. **49**, 25 (1996).
[38] U. M. B. Marconi and P. Tarazona, J. Phys.: Condens. Matter **12**, A413 (2000).
[39] M. Rex and H. Lowen, Eur. Phys. J. E **28**, 139 (2009).

[40]A. J. Archer and R. Evans, J. Chem. Phys. **121**, 4246 (2004).
[41]G. K.-L. Chan and R. Finken, Phys. Rev. Lett. **94**, 183001 (2005).
[42]A. J. Archer, J. Phys.: Condens. Matter **18**, 5617 (2006).
[43]U. Thiele, I. Vancea, A. J. Archer, M. J. Robbins, L. Frastia, A. Stannard, E. Pauliac-Vaujour, C. P. Martin, M. O. Blunt, and P. J. Moriarty, J. Phys.: Condens. Matter **21**, 264016 (2009).
[44]J. P. Boyd, *Chebyshev and Fourier Spectral Methods* (Dover, 2001).
[45]L. N. Trefethen, *Spectral Methods in MATLAB* (SIAM, 2000).
[46]L. N. Trefethen, SIAM Rev. **50**, 67 (2008).
[47]N. Hale and L. N. Trefethen, SIAM J. Sci. Comput. **46**, 930 (2008).
[48]*Theory and Simulation of Hard-Sphere Fluids and Related Systems*, Lecture Notes in Physics Vol. 753, edited by A. Mulero (Springer, Berlin Heidelberg, 2008).
[49]J. A. Barker and D. Henderson, J. Chem. Phys. **47**, 4714 (1967).
[50]J. D. Weeks, D. Chandler, and H. C. Anderson, J. Chem. Phys. **54**, 5237 (1971).
[51]S. A. Sartarelli, L. Szybisz, and I. Urrutia, Phys. Rev. E **79**, 011603 (2009).
[52]P. Tarazona and R. Evans, Mol. Phys. **52**, 847 (1984).
[53]P. Tarazona, Phys. Rev. A **31**, 2672 (1985).
[54]N. F. Carnahan and K. E. Starling, J. Chem. Phys. **51**, 635 (1969).
[55]P. Tarazona and R. Evans, Mol. Phys. **47**, 1033 (1982).
[56]J. Winkelmann, J. Phys.: Condens. Matter **13**, 4739 (2001).
[57]P. Tarazona, Mol. Phys. **52**, 81 (1984).
[58]S. Nordholm, M. Johnson, and B. C. Freasier, Aust. J. Phys. **33**, 2139 (1980).
[59]G. O. Berim and E. Ruckenstein, J. Chem. Phys. **125**, 164717 (2006).
[60]G. O. Berim and E. Ruckenstein, J. Chem. Phys. **129**, 014708 (2008).
[61]Y. Rosenfeld, Phys. Rev. Lett. **63**, 980 (1989).
[62]R. Roth, R. Evans, A. Lang, and G. Kahl, J. Phys.: Condens. Matter **14**, 12063 (2002).
[63]P. Tarazona, Physica A **306**, 243 (2002).
[64]C. Ebner, W. F. Saam, and D. Stroud, Phys. Rev. A **14**, 2264 (1976).
[65]A. J. Archer, J. Chem. Phys. **130**, 014509 (2009).
[66]M. Rauscher, J. Phys.: Condens. Matter **22**, 364109 (2010).
[67]S. Dietrich, H. L. Frisch, and A. Majhofer, Z. Phys. B: Condens. Matter **78**, 317 (1990).
[68]U. M. B. Marconi and P. Tarazona, J. Chem. Phys. **110**, 8032 (1999).
[69]J. A. Barker and D. Henderson, J. Chem. Phys. **76**, 6303 (1982).
[70]R. Baltensperger, Appl. Numer. Math. **33**, 143 (2000).
[71]J.-P. Berrut and L. N. Trefethen, SIAM Rev. **46**, 501 (2004).
[72]P. Ball and R. Evans, J. Chem. Phys. **89**, 4412 (1988).
[73]T. W. Tee and L. N. Trefethen, SIAM J. Sci. Comput. **28**, 1798 (2006).
[74]A. Hamraoui and M. Privat, Adv. Colloid Interface Sci. **149**, 1 (2009).
[75]K. T. Chu, J. Comp. Phys. **228**, 5526 (2009).
[76]B. Krauskopf, *Numerical Continuation Methods for Dynamical Systems*, edited by M. O. Hinke and J. Galn-Vioque (Springer, 2007).
[77]P. Tarazona and R. Evans, Mol. Phys. **48**, 799 (1983).
[78]R. Evans and P. Tarazona, Phys. Rev. A **28**, 1864 (1983).
[79]P. Tarazona, U. M. B. Marconi, and R. Evans, Mol. Phys. **60**, 573 (1987).
[80]A. Nold, A. Malijevský, and S. Kalliadasis, Phys. Rev. E **84**, 021603 (2011).
[81]P. Tarazona and Y. Rosenfeld, Phys. Rev. E **55**, R4873 (1997).
[82]R. Roth and S. Dietrich, Phys. Rev. E **62**, 6926 (2000).
[83]L. F. Shampine and M. W. Reichelt, SIAM J. Sci. Comput. **18**, 1 (1997).
[84]N. Savva, S. Kalliadasis, and G. A. Pavliotis, Phys. Rev. Lett. **104**, 084501 (2010).
[85]N. Savva, G. A. Pavliotis, and S. Kalliadasis, J. Fluid Mech. **672**, 358 (2011).
[86]N. Savva, G. A. Pavliotis, and S. Kalliadasis, J. Fluid Mech. **672**, 384 (2011).
[87]E. L. Allgower and K. Georg, *Introduction to Numerical Continuation Methods* (Colorado State University, 1990).
[88]A. Dhooge, W. Govaerts, Y. A. Kuznetsov, W. Mestrom, A. Riet, and B. Sautois, *MATCONT and CL MATCONT: Continuation Toolboxes in Matlab*, Utrecht University, Netherlands and Universiteit Gent, Belgium, 2006.